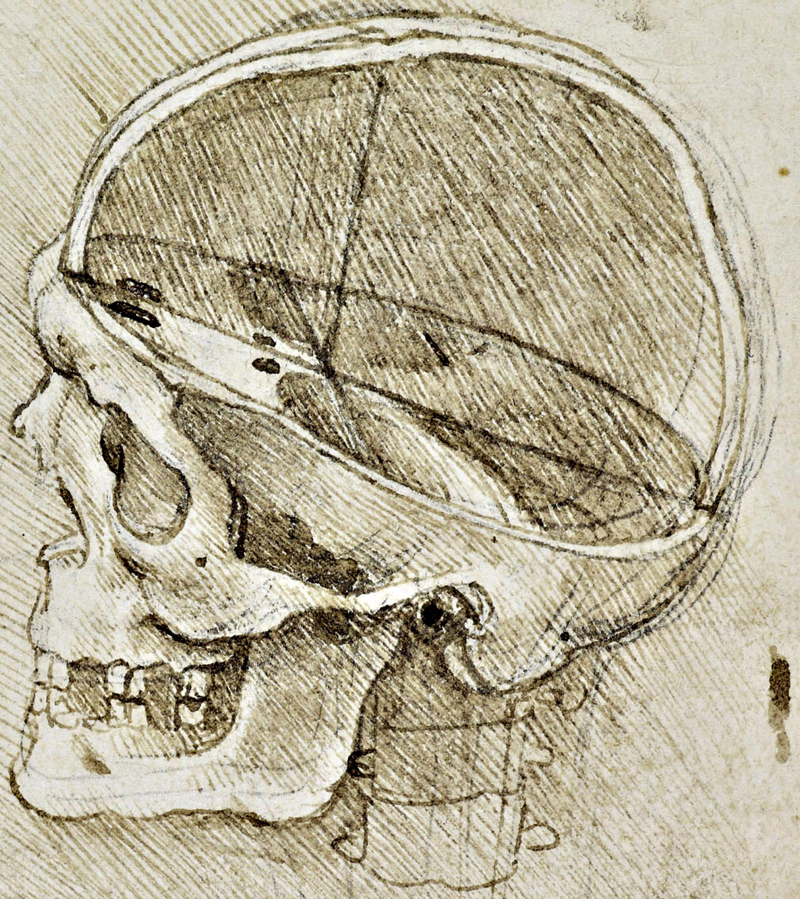
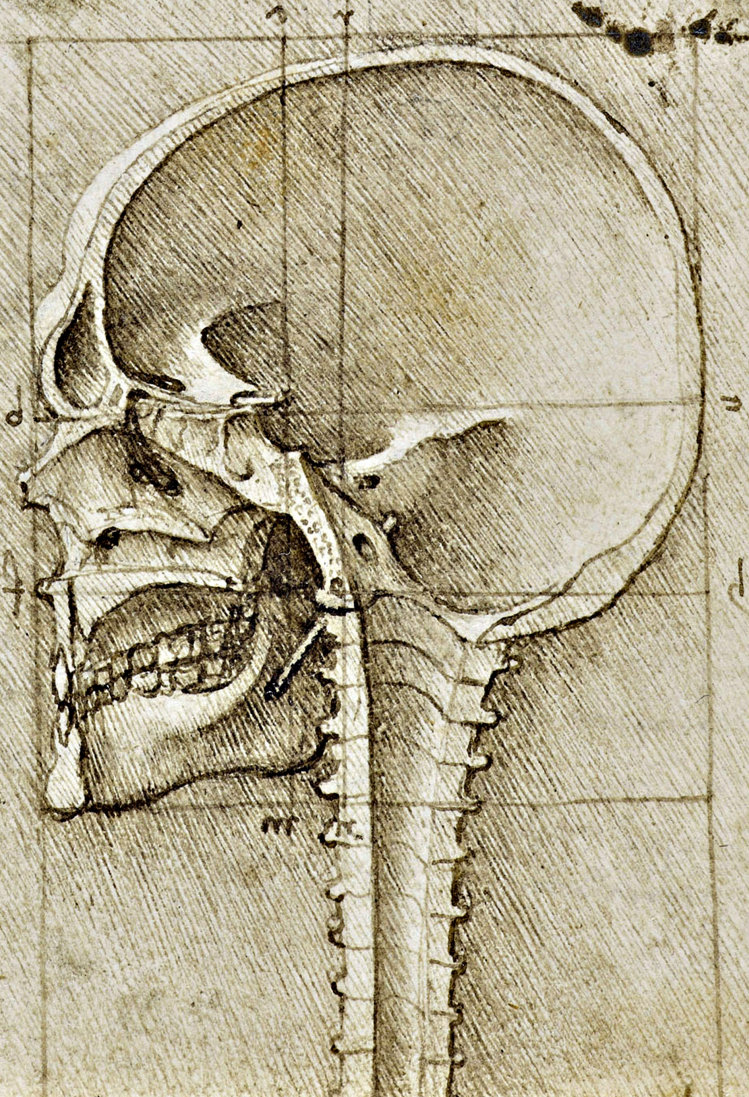


Towards quantification of
normal evolution of the
human head in order to
develop new
craniosynostosis
measurements



Handwritten text in a cursive script, likely Latin or a similar historical language, located to the left of the skull drawing.

Guido de Jong
August 2016



Handwritten text in a cursive script, likely Latin or a similar historical language, located at the bottom left of the page.

About

| | |
|--|--|
| Title | Towards quantification of normal evolution of the human head in order to develop new craniosynostosis measurements |
| Author | G.A. de Jong |
| Type | Graduate thesis for Technical Medicine |
| Affiliations | Radboudumc University of Twente |
| Chairman | Prof. dr. ir. C.H. Slump |
| Medical supervisor | Dr. H.H.K. Delye |
| Technical supervisor UT | Dr. ir. F. van der Heijden |
| Supervisor profession behaviour | Drs. P.A. van Katwijk |
| External member | Prof. dr. ir. C.H. Slump |
| Additional member | Dr. T.J.J. Maal |
| Cover Image | "The skull sectioned" by Leonardo da Vinci : Royal Collection ©Her Majesty Queen Elizabeth II. Photo by Bob Usher 9th May 2012 |

Preface

Thesis Format

Some chapters of this thesis are written in article form when applicable. This choice was made since some of the chapters have already been submitted, published as articles or are the basis of a whitepaper for a patent file application. If parts of this article are published or presented it is stated at the beginning of the chapter.

Confidential Sections

Certain sections are marked as confidential as disclosed under NDA A16-0549. These sections were marked as such to allow Radboudumc to file a patent application or (instead of or in addition to filing a patent) to find a commercial partner for exploitation of the technique described in the corresponding section. Please see the non disclosure agreement for further details. The publicly available version of this thesis will only contain the chapter titles.

Digital Media Thesis Guideline

This digital thesis contains 3D models. If you use Adobe Acrobat 9 or higher, or another PDF reader that supports embedded 3D models you can watch this content. In case you have no PDF reader that supports such content you will see a static image. The readability of this document is not compromised by viewing it with the static images alone. The 3D content is solely for an enhanced reader experience.

You can recognize movies or 3D models by the play button below the image. To view a 3D model you can press the play button. You can try this in the figure below [Figure .0.1]. The load time for 3D models after pressing the play button depends on the machine you view this digital thesis on.

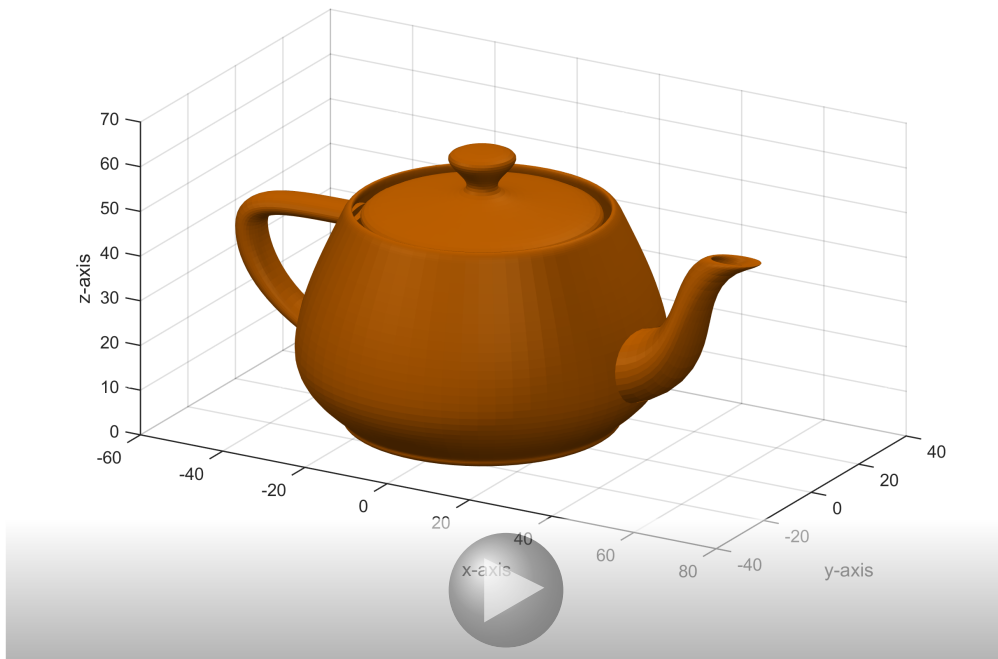


Figure .0.1: *A 3D demo figure of a teapot for testing.*

Furthermore the digital thesis also contains movies. If you use Adobe Acrobat 9 or higher, or another PDF reader that supports movies you can view the movies by clicking on the placeholder.

Abbreviations

| | |
|-------------------------|-------------------------------------|
| 3D | Three Dimensional |
| CCFP | Computed Cranial Focal Point |
| CI | Confidence Interval |
| CPU | Central Processing Unit |
| CT | Computed Tomography |
| CUDA | Compute Unified Device Architecture |
| DC | Dual Contouring |
| GPU | Graphics Processing Unit |
| HU | Hounsfield Unit |
| MC | Marching Cubes |
| MT | Marching Tetrahedra |
| MR(I) | Magnetic Resonance (Imaging) |
| NDA | Non-disclosure agreement |
| OpenCL | Open Computing Language |

Contents

| | |
|--|-----------|
| Preface | ii |
| Abbreviations | iv |
| 1 General Introduction | 1 |
| 1.1 Thesis outline | 2 |
| 2 The Computed Cranial Focal Point | 7 |
| 2.1 Introduction | 7 |
| 2.2 Materials and Methods | 8 |
| 2.2.1 Computed Cranial Focal Point Calculation | 8 |
| 2.2.2 Method Robustness Test | 8 |
| 2.2.2.1 Shape selection | 8 |
| 2.2.2.2 CCFP outcome comparison | 10 |
| 2.2.3 Patient Study | 10 |
| 2.2.3.1 Patient Study Scan selection | 10 |
| 2.2.3.2 Segmentation | 10 |
| 2.2.3.3 Registration | 11 |
| 2.2.3.4 Patient study outcome comparison | 11 |
| 2.2.4 Case Studies: Matching of a CT-scan and a 3D photo | 11 |
| 2.3 Results | 12 |
| 2.3.1 Method Robustness Test | 12 |
| 2.3.2 Patient Study | 13 |
| 2.3.3 Case Studies: Matching of a CT-scan and a 3D photo | 14 |
| 2.3.3.1 Case 1 | 14 |
| 2.3.3.2 Case 2 | 14 |
| 2.4 Discussion | 15 |
| 2.5 Conclusion | 17 |
| 2.6 Appendix | 18 |
| 2.6.1 CCFP Calculation | 18 |

| | | |
|----------|--|-----------|
| 2.6.2 | Calculation Software | 18 |
| 3 | ISO-Surface Extraction for CCFP calculations | 21 |
| 3.1 | Introduction | 21 |
| 3.2 | Criteria of ISO-surface algorithms | 21 |
| 3.3 | History of ISO-surface algorithms | 22 |
| 3.4 | Selection of ISO-surface algorithms | 23 |
| 3.5 | Discussion | 24 |
| 3.6 | Conclusion | 25 |
| 4 | Real-Time Mesh Simplification Using Heterogeneous Computing | 29 |
| 4.1 | Confidential | 29 |
| 5 | Computed Cranial Focal Point in the Adult Population Revised | 31 |
| 5.1 | Introduction | 31 |
| 5.2 | Materials and Methods | 31 |
| 5.2.1 | Segmentation | 32 |
| 5.2.2 | Registration | 32 |
| 5.2.3 | Mesh Simplification | 33 |
| 5.2.4 | Sampling | 33 |
| 5.2.5 | Computed Cranial Focal Point Calculation | 34 |
| 5.2.6 | Hardware and Software | 34 |
| 5.2.7 | Evaluation | 34 |
| 5.3 | Results | 34 |
| 5.3.1 | Segmentation, Registration, Simplification and Sampling | 34 |
| 5.3.2 | Calculated Computed Cranial Focal Point | 35 |
| 5.3.2.1 | Effect of Simplification and Sampling | 35 |
| 5.4 | Discussion | 40 |
| 5.4.1 | CCFP result difference | 40 |
| 5.4.2 | New CCFP Calculation Method | 40 |
| 5.5 | Conclusion | 41 |
| 5.6 | Appendix | 41 |
| 5.6.1 | Improving the CCFP Calculation | 41 |
| 5.6.1.1 | Original CCFP Calculation | 41 |
| 5.6.1.2 | Improved CCFP Calculation | 43 |
| 6 | Computed Cranial Focal Point Evolution in a Normal Pediatric Population | 45 |
| 6.1 | Introduction | 45 |

| | | |
|----------|---|-----------|
| 6.2 | Materials and Methods | 46 |
| 6.2.1 | Patient Study Scan selection | 46 |
| 6.2.2 | Segmentation, Registration, Sampling | 47 |
| 6.2.3 | CCFP Calculation | 48 |
| 6.2.4 | Statistical analysis | 48 |
| 6.3 | Results | 48 |
| 6.3.1 | Trend interpretation | 49 |
| 6.3.2 | Statistical Analysis | 50 |
| 6.4 | Discussion | 50 |
| 6.5 | Conclusion | 51 |
| 7 | Radiation-free 3D head shape and volume evaluation after endoscopically assisted strip craniectomy followed by helmet therapy for trigonocephaly | 53 |
| 7.1 | Introduction | 53 |
| 7.2 | Materials and Methods | 54 |
| 7.2.1 | Orientation and Resampling | 55 |
| 7.2.2 | Volume Analysis | 57 |
| 7.2.2.1 | Statistical Analysis | 57 |
| 7.2.3 | Shape Analysis | 57 |
| 7.3 | Results | 58 |
| 7.3.1 | Volume Analysis | 58 |
| 7.3.1.1 | Comparison of anterior growth percentages | 60 |
| 7.3.1.2 | Statistical Analysis | 61 |
| 7.3.2 | Shape Analysis | 62 |
| 7.3.2.1 | Absolute Shape | 62 |
| 7.3.2.2 | Normalized Shape | 64 |
| 7.4 | Discussion | 66 |
| 7.5 | Conclusion | 68 |
| 7.6 | Appendix | 68 |
| 7.6.1 | Orientation Procedure | 68 |
| 7.6.1.1 | CT-scans | 68 |
| 7.6.1.2 | 3D Photos | 69 |
| 8 | General Discussion | 73 |
| 9 | Acknowledgments | 77 |

1 | General Introduction

Craniosynostosis is defined by the premature fusion of cranial sutures with an incidence estimated at 1 in 2000 to 1 in 2500 live births [1]. Classification of isolated craniosynostosis depends on the suture or sutures that are fused [2]. Scaphocephaly occurs with sagittal synostosis and is characterized by long and narrow head growth. Trigonocephaly is caused by the metopic synostosis resulting in a triangular shaped forehead. Plagiocephaly can either occur in anterior form (coronoal synostosis) or posterior form (lambdoid synostosis) with flattening of the affected side of the head. Brachycephaly is a form of craniosynostosis where both of the coronal sutures are fused resulting in a flat elevated forehead. Oxycephaly occurs when both coronal and sagittal sutures are fused. Craniosynostosis can also occur as a part of a syndrome like Crouzon, Apert, or Pfeiffer [2].

Untreated craniosynostosis can result in increased intracranial pressure as well as impact mental development [2]. There is also an aesthetics aspect to perform an intervention for craniosynostosis. Treatment of craniosynostosis usually occurs by surgery [2, 3]. Each form of craniosynostosis requires different surgical strategies. Multiple strategies can also be present for a single form of craniosynostosis. For instance the open cranial vault reconstruction or (endoscopic) suturectomy with spring- or /helmet therapy for trigonocephaly [4, 5, 6]. The endoscopic suturectomy surgery was introduced as an alternative to the open surgery for sagittal craniosynostosis [7]. In the following years this technique was also adopted for other forms of craniosynostosis, including metopic suture craniosynostosis [8, 9]. However objective monitoring or comparison between techniques is limited.

Objective monitoring of the effects of craniosynostosis surgery relies heavily on the use of skull growth measurement. 3D Skull measurements have become more widely used [10, 11, 12, 13]. These newer methods primarily rely on defining 3D parameters of the skull using CT-scans, involving ionizing radiation. Because this introduces an increased radiation dose during longitudinal follow up, alternative techniques like 3D photogrammetry have been proposed to monitor 3D skull parameters [14, 15, 16, 17, 16, 17, 18]. These techniques are limited to capturing the soft tissue surfaces. It has yet to be validated how the captured soft tissue correlates to the bony skull. Validation is difficult primarily due to the lack of consistent

markers to overlay and match sequential 3D photos for growth monitoring. The current golden standard for overlaying skulls uses the sella turcica, dorsum sella or a nearby structure as skull to skull overlay point due to the assumption that these structures remain immobile during skull growth [19]. However these structures cannot be captured on 3D photos.

The goal of this thesis is to create a method for quantification of the human head evolution based on 3D photogrammetry. Such quantification allows to objectively describe the morphology of the head. Using objective quantification furthermore allows comparison between human heads, or follow-up of the longitudinal evolution of heads. This is of interest after craniostyosis interventions. Thus the final goal is to use this new method for longitudinal follow-up after craniostyosis interventions.

1.1. Thesis outline

Using 3D photos for longitudinal follow-up after craniostyosis interventions requires a measure for overlaying and matching sequential 3D photos. In the following chapter [Section 2] a new method is proposed using the “Computed Cranial Focal Point” (CCFP) for overlaying CT-scans and 3D Photos with respect to the sella turcica. The robustness of the CCFP is tested in synthetic models. The mean position and standard deviation of the CCFP in the sella turcica-nasion orientation is determined for the adult population. Finally the CCFP is used in the overlaying of a set of 3D photos with CT-scans of children suspected for craniostyosis.

For the initial CCFP computation certain compensations had to be made. One of the compensations was the volume reduction prior to ISO-surface extraction to reduce computation time. However this technique of volume reduction is slow and also results in loss of details. ISO-surface extraction creates a 3D surface from a set of voxels where the voxel values equal a certain ISO-value. There are many methods for ISO-surface extraction that differ in speed as well as surface properties like the amount of details, amount of faces (triangles) and the occurrence of noise or errors. The CCFP computation becomes slower if an extracted surface has more faces. However less faces can result in an inaccuracy of the surface as well as the CCFP position. Thus an optimum number of faces and details are needed for the CCFP computation. A set of ISO-surface extraction methods are explored in [Section 3]. In addition a scalable mesh simplification technique is introduced in [Section 4]. The combinations of these chapters result in a fast scalable detail preserving ISO-surface extraction and simplification combination that can be used for this study and CCFP computations in CT-scans.

In [Section 5] a selection of compromises from the original CCFP computation are tackled. In addition the effect of sampling of meshes on the CCFP position is also explored. Sampling is used to further reduce the CCFP computation time. This doubles to mimic the effects of using

3D photos that by default have less faces in a mesh compared to surfaces of CT-scans.

With the growth of the human skull it could be possible that the CCFP also shows a change in position relative to the sella turcica over time. In order to quantify this effect a set of CT-scans of pediatric patients are analyzed in [Section 6] similar to that of the adult set from [Section 5]. The CT-scans of these pediatric patients are group by age to determine the change of the CCFP position over time.

Using the CCFP evolution as correction values in 3D photos it is possible to use these photos for longitudinal evaluation of the head shape and volume changes after craniostylosis interventions. This resulted in the radiation-free 3D head shape and volume evaluation after endoscopically assisted strip craniectomy followed by helmet therapy for trigonocephaly in [Section 7].

Combining these techniques results in a thesis describing the path towards quantification of normal evolution of the human head in order to develop new craniostylosis measurements. Finally this thesis describes a longitudinal follow-up after endoscopically assisted strip craniectomy using the quantification method.

References

- [1] Bethany J Slater et al. "Cranial sutures: a brief review." In: *Plastic and reconstructive surgery* 121.4 (2008), 170e–8e. ISSN: 1529-4242. DOI: 10.1097/01.prs.0000304441.99483.97.
- [2] D. Renier et al. "Management of craniostyloses". In: *Child's Nervous System* 16.10-11 (2000), pp. 645–658. ISSN: 02567040. DOI: 10.1007/s003810000320.
- [3] Jayesh Panchal and Venus Uttchin. "Management of craniostylosis". In: *Plastic and reconstructive surgery* 111 (2003), 2032–2048; quiz 2049. ISSN: 0032-1052. DOI: 10.1097/01.PRS.0000056839.94034.47.
- [4] Sassan Keshavarzi et al. "Variations of Endoscopic and Open Repair of Metopic Craniostylosis". In: *Journal of Craniofacial Surgery* 20.5 (2009), pp. 1439–1444. ISSN: 1049-2275. DOI: 10.1097/SCS.0b013e3181af1555.
- [5] J. Hinojosa. "Endoscopic-assisted treatment of trigonocephaly". In: *Child's Nervous System* 28.9 (2012), pp. 1381–1387. ISSN: 02567040. DOI: 10.1007/s00381-012-1796-7.
- [6] Fatma Ozlen et al. "Surgical treatment of trigonocephaly: technique and long-term results in 48 cases." In: *Journal of neurosurgery. Pediatrics* 7.3 (2011), pp. 300–10. ISSN: 1933-0715. DOI: 10.3171/2010.12.PEDS10359.

- [7] D F Jimenez and C M Barone. *Endoscopic craniectomy for early surgical correction of sagittal craniosynostosis*. 1998. DOI: 10.3171/jns.1998.88.1.0077. URL: <http://www.ncbi.nlm.nih.gov/pubmed/9420076>.
- [8] David F Jimenez et al. "Early management of craniosynostosis using endoscopic-assisted strip craniectomies and cranial orthotic molding therapy." In: *Pediatrics* 110.1 Pt 1 (2002), pp. 97–104. ISSN: 0031-4005. DOI: 10.1542/peds.110.1.97.
- [9] C M Barone and D F Jimenez. "Endoscopic craniectomy for early correction of craniosynostosis." In: *Plastic and reconstructive surgery* 104.7 (1999), 1965–73; discussion 1974–5. ISSN: 0032-1052. DOI: 10.3171/jns.1998.88.1.0077.
- [10] JR Marcus, LF Domeshek, and Rajesh Das. "Objective three-dimensional analysis of cranial morphology." In: *Eplasty* 8 (2007), pp. 175–187.
- [11] Jeffrey R Marcus et al. "Use of a three-dimensional, normative database of pediatric craniofacial morphology for modern anthropometric analysis." In: *Plastic and reconstructive surgery* 124.6 (2009), pp. 2076–84. ISSN: 1529-4242. DOI: 10.1097/PRS.0b013e3181bf7e1b.
- [12] Nikoo R Saber et al. "Generation of normative pediatric skull models for use in cranial vault remodeling procedures." In: *Child's nervous system : ChNS : official journal of the International Society for Pediatric Neurosurgery* 28.3 (2012), pp. 405–10. ISSN: 1433-0350. DOI: 10.1007/s00381-011-1630-7.
- [13] Hans Delye et al. "Creating a normative database of age-specific 3D geometrical data, bone density, and bone thickness of the developing skull: a pilot study". In: *Journal of Neurosurgery: Pediatrics* 16.6 (2015), pp. 687–702. ISSN: 1933-0707. DOI: 10.3171/2015.4.PEDS1493.
- [14] Jan-Falco Wilbrand et al. "Objectification of cranial vault correction for craniosynostosis by three-dimensional photography." In: *Journal of cranio-maxillo-facial surgery : official publication of the European Association for Cranio-Maxillo-Facial Surgery* 40.8 (2012), pp. 726–30. ISSN: 1878-4119. DOI: 10.1016/j.jcms.2012.01.007.
- [15] Douglas R McKay et al. "Measuring cranial vault volume with three-dimensional photography: a method of measurement comparable to the gold standard." In: *The Journal of craniofacial surgery* 21.5 (2010), pp. 1419–22. ISSN: 1536-3732. DOI: 10.1097/SCS.0b013e3181ebe92a.
- [16] Robert Toma et al. "Quantitative morphometric outcomes following the Melbourne method of total vault remodeling for scaphocephaly." In: *The Journal of craniofacial surgery* 21.3 (2010), pp. 637–43. ISSN: 1536-3732. DOI: 10.1097/SCS.0b013e3181d841d9.

- [17] P. Meyer-Marcotty et al. "Three-dimensional analysis of cranial growth from 6 to 12 months of age". In: *The European Journal of Orthodontics* 36.March 2013 (2013), cjt010-. ISSN: 0141-5387. DOI: 10.1093/ejo/cjt010.
- [18] Heidrun Schaaf et al. "Three-dimensional photographic analysis of outcome after helmet treatment of a nonsynostotic cranial deformity." In: *The Journal of craniofacial surgery* 21.6 (2010), pp. 1677–1682. ISSN: 1049-2275. DOI: 10.1097/SCS.0b013e3181f3c630.
- [19] Arne Björk. "Cranial base development: a follow-up x-ray study of the individual variation in growth occurring between the ages of 12 and 20 years and its relation to brain case". In: *American Journal of Orthodontics* (1955). DOI: 10.1016/0002-9416(55)90005-1.

2 | The Computed Cranial Focal Point

This chapter was previously published: [de Jong G a., Maal TJJ & Delye H, The computed cranial focal point. *J Cranio-Maxillofacial Surg*, 43:1737-1742, 2015. doi: 10.1016/j.jcms.2015.08.023]. There are minor deviations between the this chapter and the publication for a better reading experience for this thesis.

Parts of this chapter were presented or are to be presented at the following events:

- Poster presentation at EANS 2014, Prague (Czech republic), 15th European Congress of Neurosurgery, 12-17 October 2014
- Oral presentation at NVSCA 2014, Rotterdam (Netherlands), 29e najaarsvergadering van de Nederlandse Vereniging voor Schisis en Craniofaciale Afwijkingen, 15 November 2014
- Oral presentation at ECC 2015, Gothenburg (Sweden), 1th European Craniofacial Congress, 24-27 June 2015
- Oral presentation at ESPN 2016, Paris (France), 25th Congress of the European Society for Pediatric Neurosurgery, 8-11 May 2016
- Poster presentation at ISPN 2016, Kobe (Japan), 44th Annual Meeting of the International Society for Pediatric Neurosurgery, 23-27 October 2016

2.1. Introduction

In the general introduction [Section 1] we introduce one of the main problems of overlaying and matching 3D Photos for growth monitoring without knowledge of the bony structures.

We propose a new method using the “Computed Cranial Focal Point” (CCFP). The CCFP is the point in the cranium where all the surface normals of the skin or skull tend to intersect. The CCFP can be calculated for any spherical body like the skull or soft tissue surface of the head. The relative position from the sella turcica to the CCFP can be determined for the skin (CCFP-skin) and the skull (CCFP-skull) using CT-scans. In this study, we investigate how these

points can be used for sequential photogrammetry matching, by defining the relation between the CCFP -skin and the CCFP-skull and their relative position to the sella turcica.

With the use of the CCFP we aim for a radiation free method to assist in objective sequential measurements of skull growth, to be used in craniosynostosis follow-up. This to reduce the need for CT-scans and thus to reduce the radiation exposure to pediatric patients with craniosynostosis.

2.2. Materials and Methods

We developed the calculation of the CCFP and tested the robustness of this calculation method. Secondly, we performed an explorative patient study to define the relation between the CCFP-skin and the CCFP-skull and their relative position to the sella turcica. Finally, we used the CCFP-skin to match a CT-scan and 3D photo in two separate cases to evaluate the potential of the CCFP for matching a CT-scan and 3D photo.

2.2.1. Computed Cranial Focal Point Calculation

The CCFP can be calculated by determining the mean virtual intersection point of all the surface normals. All these intersection points combined create a point cloud in the cranium with a center point and spread (CCFP σ). In depth calculation of the CCFP can be found in Appendix 2.6.

Please see [Section 5.6.1] for the improved CCFP Calculation.

2.2.2. Method Robustness Test

2.2.2.1. Shape selection

The method robustness test was done using a set of predefined shapes as meshes (triangulated objects). Since this is a new method no predefined set of shapes to benchmark the method exists. The shapes were chosen to distinguish the effect on the CCFP and CCFP σ caused by the conditions that could appear in real world cases. All the shapes are spherically centered around the origin (0,0,0). The x-direction is from medial to lateral as seen from the left side, the y-direction from caudal to cranial and the z-direction from anterior to posterior. We used approximately 50.000 triangles per shape for optimum computation time versus accuracy.

The CCFP and CCFP σ of these shapes were calculated and compared with known values to determine the calculation accuracy. The CCFP coordinates are defined relative to the origin

(0, 0, 0) in mm as xyz. The $CCFP\sigma$ is also defined in mm as xyz.

One shape is a sphere with a radius of 9.6 cm. There also were 4 hemi-ellipsoid shapes originating from a hemi-ellipsoid with a height and length radius of 9.6 cm and a width radius of 7.7 cm [Figure 2.2.1(a)]. These measures were chosen to approximate the average human head size. The other 3 hemi-ellipsoid shapes were either asymmetrical cut to remove approximately 20% of the total surface at 15 degrees pitch and 5 degrees roll [Figure 2.2.1(b,d)] and/or irregularly deformed up to 2.0 cm of the original [Figure 2.2.1(c,d)]. This is to mimic irregular skull shapes and partial missing data as could occur on a CT-scan. There were also two other shapes based on the hemi-ellipsoid resembling respectively trigonocephaly [Figure 1(e)] and scaphocephaly [Figure 2.2.1(f)].

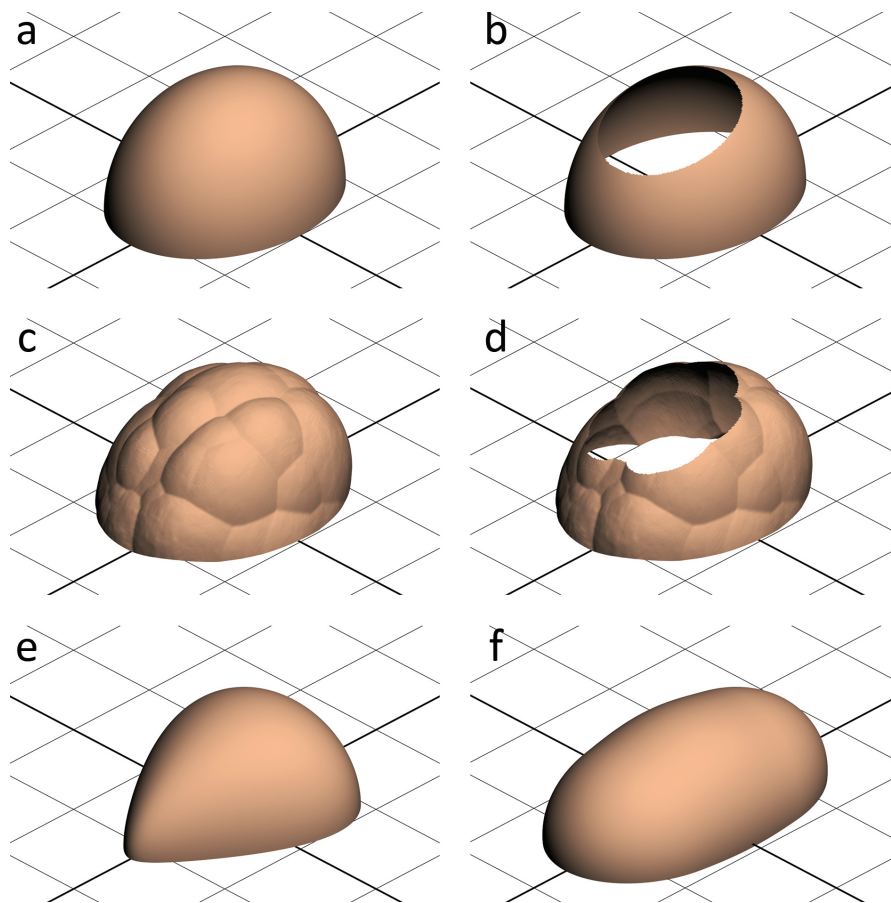


Figure 2.2.1: A selection of the meshes that have been used in the Method Robustness Test. **a** (Top Left): hemi-ellipsoid, **b** (Top Right): hemi-ellipsoid cut, **c** (Middle Left): hemi-ellipsoid deformed, **d** (Middle Right): hemi-ellipsoid deformed and cut, **e** (Bottom Left): hemi-ellipsoid trigonocephaly, **f** (Bottom Right): hemi-ellipsoid scaphocephaly

2.2.2.2. CCFP outcome comparison

The sphere, full hemi-ellipsoid and the cut hemi-ellipsoid shapes have a known geometric focal point at the origin. The deformed hemi-ellipsoids shapes and the trigonocephaly- and scaphocephaly- shapes are constructed around the origin but do not necessarily have a geometric focal point at the origin. The position of the CCFP relative to the origin and the CCFP σ to (0,0,0) for the sphere is caused by polygon inaccuracy and the calculation itself. A similar comparison for the cut and full shapes give the difference caused by removing a part of the shape. Comparing the CCFP and CCFP σ between the deformed and normal shapes gives the difference caused by deformation.

The trigonocephaly- and scaphocephaly- shaped hemi-ellipsoid shapes originated from the hemi-ellipsoid with a known focal point at the origin and have been freeform scaled. The difference of the CCFP and the relative CCFP difference compared to the normal hemi-ellipsoid give the error caused by variation.

2.2.3. Patient Study

2.2.3.1. Patient Study Scan selection

For the explorative study, we used scans from patients that underwent a cranial CT-scan in the ER in RadboudUMC between June 2013 and June 2014. Scans showing cranial trauma or structural pathologies were excluded resulting in a group of 36 patients aged 18-65 y.o. (mean 42,6 y.o.) of which 19 were female. The scans were made with a Toshiba Aquilion ONE using a pixel spacing of 0.432 mm and a slice thickness of 0.5 mm with a slice resolution of 512x512 by 302 to 376 slices. The scans were anonymized in accordance to local rules from the institutional board of the academic hospital.

2.2.3.2. Segmentation

All the CT-scans were segmented prior to the calculation of the CCFP to obtain the outer surface of the skull and the skin of the head as a mesh. A threshold of -150 HU for the skin and 500 HU for the bone was used and tweaked per scan for the optimum segmentation. Filters were applied removing small artifacts outside the head and to fill any surrounded structures. The resulting volume data was resized to create voxels of approximately 1x1x1 mm. Segmentation was applied from above the supraorbital process to the lowest possible point on the parietal bone. The mesh was made by using Matlab's [20] built-in 'isosurface' function.

2.2.3.3. Registration

The meshes underwent a translation so that the position of the sella turcica was aligned to the origin (0, 0, 0). Scaling was applied so that 1 unit in the mesh-space equals 1 mm.

The meshes were aligned with the sella nasion plane crossed with the horizon of the sphenoid at the sella turcica as the horizontal plane. Axis were directed so that sella to cranial is the positive y-direction, the sella to posterior is the positive z-direction, and the right to left is the positive x-direction. All triangles of the mesh $y < -5\text{mm}$ of the sella turcica were omitted in further calculations.

2.2.3.4. Patient study outcome comparison

The main goal of the patient study is to investigate the relation between the CCFP-skull and CCFP-skin. The secondary goal is to determine the relation between the CCFP-skull/CCFP-skin and the sella turcica.

2.2.4. Case Studies: Matching of a CT-scan and a 3D photo

The first case was a 9 month old female suspected of craniosynostosis of which a 3D photo was made. A CT-scan followed 3 weeks after the photo disproving craniosynostosis. The second case was a 3 month old female patient with suspected craniosynostosis of which a CT-scan was made proving trigonocephaly. For further evaluation a 3D photo of this patient was made 6 weeks after the CT-scan. Both cases were individually used for matching the CT-scan and 3D photo using the CCFP.

In prospect to the results of the patient study we can say that the relative position between sella turcica, CCFP-skin and CCFP-skull is predictable. Due to this property of the CCFP values we can use the CCFP for matching. Hence the CCFP-skin of a 3D photo and CT-scan was used. Per case the CCFP-skin was calculated for both the CT-scan and 3D photo. We aligned and rotated the CT-scan similar to that of the patient study. We transformed the 3D photo with the CCFP-skin to the CCFP-skin of the CT-scan. The 3D photo was then manually rotated to match the CT-scan using the CCFP as a pivot.

We calculated the difference between the two meshes using raycasting [21]. A raycast will be performed from the 3D photo with the origin in each vertex and the direction equal to the normal of each vertex. The normal of the vertex is the average normal of the triangles it is a part of. For each raycast the absolute difference between the hitpoints of the CT-scan skin and 3D photo is expressed as the matching difference per triangle. The raycasting was accelerated using OpenCL [22]. We determined the absolute mean difference, standard deviation and the maximum difference and the location of the maximum difference for the raycasting.

2.3. Results

2.3.1. Method Robustness Test

The method robustness test focused on the accuracy of the CCFP for a known focal point and the spread of the CCFP σ for various meshes. All given CCFP coordinates and CCFP σ standard deviations are presented in [Table 2.3.1].

Table 2.3.1: *The distance in for X, Y, Z from 0,0,0 to the CCFP and the standard deviation of X,Y,Z for the test models in mm.*

| Structure | CCFP (mm) | | | CCFP σ (mm) | | |
|---------------------------------|-----------|------|------|--------------------|-------------|-------------|
| | X | Y | Z | $\sigma(X)$ | $\sigma(Y)$ | $\sigma(Z)$ |
| Sphere | 0.0 | 0.0 | 0.0 | 0.01 | 0.01 | 0.01 |
| Hemi-ellipsoid | 0.0 | 7.7 | 0.0 | 8.3 | 2.7 | 5.6 |
| Hemi-ellipsoid cut | 0.8 | 7.0 | 1.1 | 9.2 | 2.5 | 6.0 |
| Hemi-ellipsoid deformed | -0.7 | 9.8 | 0.8 | 9.9 | 8.4 | 9.9 |
| Hemi-ellipsoid deformed and cut | -1.6 | 10.0 | 0.9 | 9.6 | 7.8 | 11.7 |
| Hemi-ellipsoid trigonocephaly | 0.0 | -5.6 | 10.7 | 9.5 | 5.7 | 9.7 |
| Hemi-ellipsoid scaphocephaly | 0.0 | -6.2 | -0.1 | 12.1 | 24.5 | 7.2 |

In the sphere there was no measurable deviation for the CCFP and a (0.01, 0.01, 0.01) mm spread for the CCFP σ . This can be considered negligible in CT-scans with a voxel spacing size of 0.5 mm^3 .

The full, cut, and deformed hemi-ellipsoid shapes have a predominant y-component for the CCFP around 8 mm and small x- and z-components (ranging from -0.7 to 1.1 mm). Do note that the CCFP does not have to represent the geometrical focus. The distance between the full and the cut hemi-ellipsoid is 1.5 mm and between the full and deformed hemi-ellipsoid is 2.4 mm . The distance between the deformed hemi-ellipsoid and the deformed and cut hemi-ellipsoid is 0.9 mm . Removing approximately 20% of the surface results in a smaller difference of the CCFP than applying up to 2 cm deformations to the surface. In case of deformations the difference caused by the cut is almost similar to the cut alone.

The spread for the full, cut and deformed hemi-ellipsoid shapes ranges from 2.5 to 11.7 mm . The full and cut versions have a predominant spread in the x- and z-direction. The y-direction has the smallest spread in these cases. The deformations primarily add to the spread in the y- and z-direction and are even more present in the z-direction when cut.

The trigonocephaly hemi-ellipsoid has a CCFP of (0.0, -5.6, 10.7). This deviates 17.1 *mm* from the full hemi-ellipsoid and is most present in the *y*- and *z*-direction. The scaphocephaly hemi-ellipsoid in contrast has a CCFP of (0.0, -6.2, -0.1) which only significantly deviates in the *y*-direction from the full hemi-ellipsoid (13.9 *mm*).

The spread for the trigonocephaly primarily deviates from the full hemi-ellipsoid in the *y*- and *z*-direction. The spread for the scaphocephaly deviates in all directions with the highest deviation in the *z*-direction up to 24.5 *mm*.

2.3.2. Patient Study

The results of the CT-scans can be found in [Table 2]. The CCFP (*mm*) is expressed as relative to the sella turcica (0, 0, 0) in the sella-nasion orientation. The average CCFP-skull is at (-0.4, 28.9, 18.0) with a σ (0.5, 4.5, 4.4) while the CCFP-skin is at (0.0, 27.1, 19.4) with a σ (0.6, 4.6, 3.9). Using a Shapiro-Wilk test resulted in proven normal distributions in the *x*- and *y*-direction with CCFP-skull *p*-values of (0.226, 0.452, 0.000) and CCFP-skin *p*-values of (0.388, 0.526, 0.001).

The difference between the σ of the CCFPs is in sub-millimeter scale. The mean CCFP differs (-0.1, 1.9, -1.4) from skull to skin with a maximum σ of 1.4 *mm* and a maximum 95% CI of mean \pm 0.6 *mm*.

Table 2.3.2: *The mean CCFP, standard deviation and 95% CI for the population of 36 patients for the skull, skin and difference between the skull and skin (Δ) in mm.*

| CCFP | Mean (<i>mm</i>) | σ | 95%CI |
|---------------------------|--------------------|----------|-------------|
| Skull _{<i>x</i>} | 0.0 | 0.5 | -0.3 – 0.1 |
| Skull _{<i>y</i>} | 29.9 | 4.6 | 28.3 – 31.5 |
| Skull _{<i>z</i>} | 18.6 | 4.2 | 17.2 – 20.0 |
| Skin _{<i>x</i>} | 0.1 | 0.6 | -0.1 – 0.3 |
| Skin _{<i>y</i>} | 27.9 | 4.9 | 26.3 – 29.6 |
| Skin _{<i>z</i>} | 20.0 | 3.6 | 18.7 – 21.2 |
| Δ_x | -0.1 | 0.7 | -0.4 – 0.1 |
| Δ_y | 1.9 | 1.7 | 1.4 – 2.5 |
| Δ_z | -1.4 | 1.2 | -1.7 – -0.9 |

2.3.3. Case Studies: Matching of a CT-scan and a 3D photo

2.3.3.1. Case 1

Visual representation of the registration in 3D shows a nicely matched overlay [Figure 2.3.1]. The colors represent the difference between the 3D photo and CT-scan. The overlay shows the origin at the sella turcica as obtained from the CT-scan. A blue circle at the top shows the position of the maximum difference as caused by the hairnet.

The absolute average raycast difference was 0.7 mm with a standard deviation of 1.1 mm . The biggest difference was 6.72 mm at the bulge of the hairnet but did not seem to significantly impact the average.

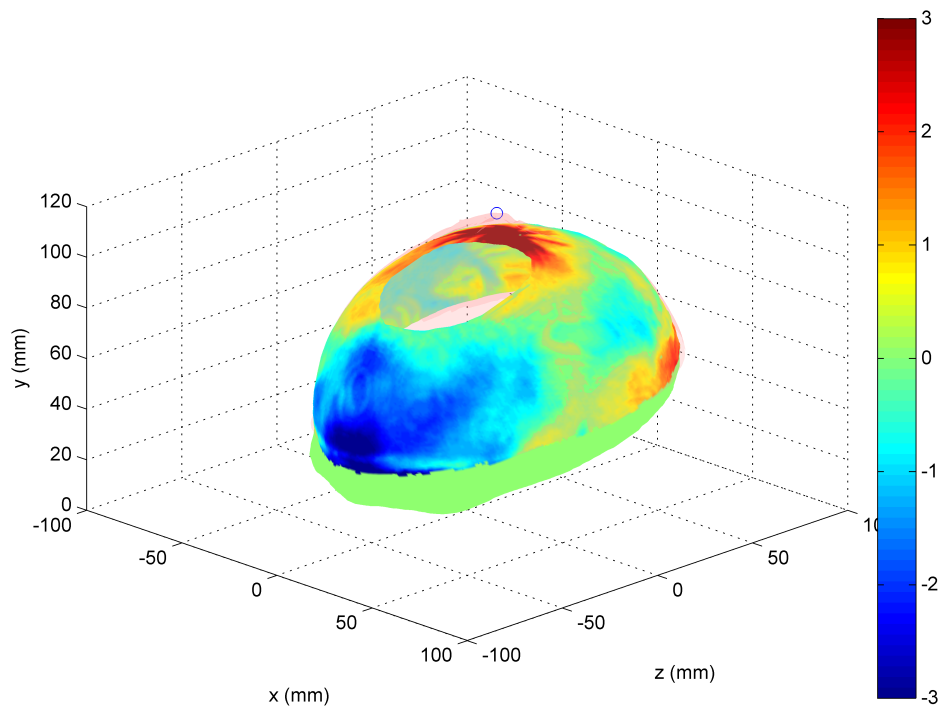


Figure 2.3.1: *Overlaying and distance map of a 3D photo and CT-scan using CCFP-skin matching and manual rotation in a 9 month old female patient.*

2.3.3.2. Case 2

The visual representation of the registration in 3D shows a nicely matched overlay [Figure 2.3.2] with the origin at the sella turcica as obtained from the CT-scan. A blue circle at the top shows

the position of the maximum difference as caused by the hairnet. Again the colors represent the difference between the 3D photo and CT-scan.

The absolute average raycast difference was 2.3 *mm* with a standard deviation of 1.1 *mm*. The biggest difference was 6.44 *mm* at the bulge of the hairnet at the back of the head.

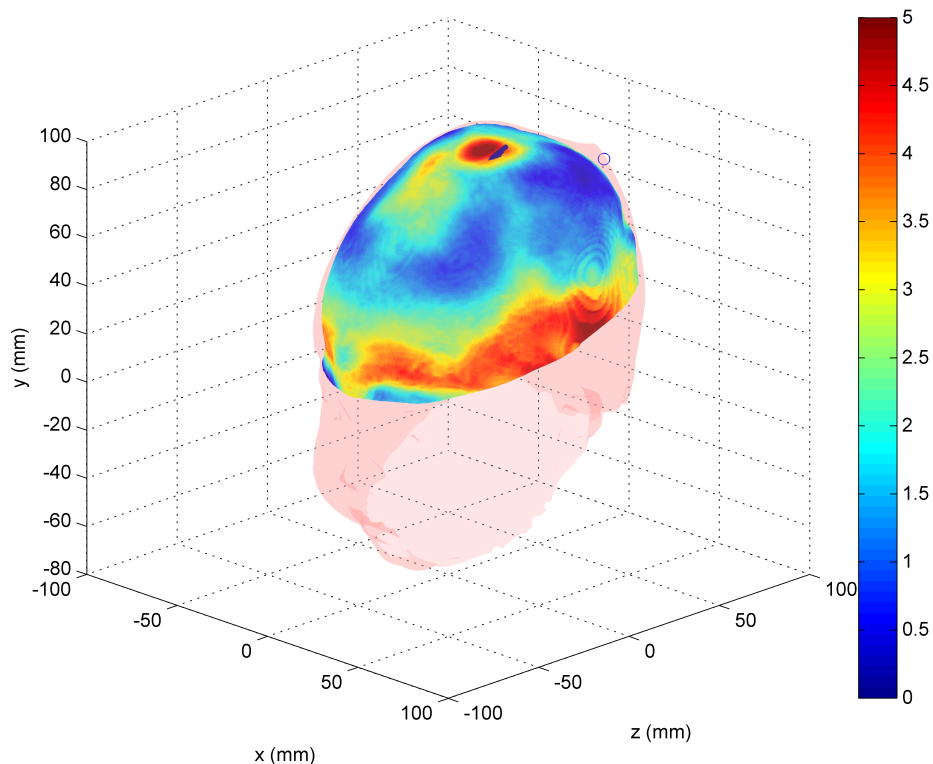


Figure 2.3.2: *Overlaying and distance map of a 3D photo and CT-scan using CCFP-skin matching and manual rotation in a 3 month old female patient.*

2.4. Discussion

The method robustness test showed that the CCFP calculation is robust against missing data and deformation in hemi-ellipsoid shapes. The part of the head used for these calculations is roughly hemi-ellipsoid in healthy patients but shows different expressions in patients with craniosynostosis. The craniosynostosis shapes showed a deviant CCFP position as compared to the other cases. This makes it possibly useful for classifying these conditions but less useful for comparison between these and healthy heads without the use of additional reference points. Thus finding other reference points that can be related to the sella turcica or using only a partial CCFP calculation by excluding the affected part of the head might overcome this issue.

The segmentation process was done in Matlab [20] resulting in some limitations. Especially when CT scan was performed with considerable head flexion, segmentation and registration resulted in a smaller usable section for CCFP calculation. Missing data did not influence the CCFP calculation significantly in the robustness test, however accuracy improves utilizing all data. Changing the segmentation process in Matlab could resolve this issue. Another option is using software like ITK-snap to handle the segmentation [23].

The patient study consisted of 36 patients and was of an explorative nature. Hence the study only gives an indication of the distribution of the CCFP among the adult population. Using a larger sample results in even more accuracy, although this study showed a small 95% CI spread for CCFPs. Yet the few millimeter 95% CI spread for CCFPs suggest that the mean position for the CCFPs between individuals is at about the same position relative to the sella turcica. The 95% CI sub-millimeter spread for the mean difference between the CCFP-skin and CCFP-skull suggests that the position relative to each other is predictable.

The case studies of matching 3D photos with CT-scans using the CCFP showed a very high agreement. A follow-up study is needed to show pitfalls or problems during this process. Although the absolute average difference is bigger than in first case, the standard deviation of the difference is almost equal in both cases. This can be explained by the time between the CT-scan and 3D photo as well as the order in which these were taken. In the first case the 3D photo was made prior to the CT-scan which added the hairnet to the overall 3D photo volume but where growth added to the CT-scan volume and thus somewhat compensating each other's additional volume. In the second case the CT-scan came prior to the 3D photo which allowed both the hairnet and the additional growth time (3 versus 6 weeks) to add to the volume of the 3D photo. Therefore it is to be expected that there was a bigger absolute average difference compared to the first case. Taking this in consideration as well as the near equal standard deviation and the visual inspection suggests that in both cases the overlay was performed with equal accuracy. Finally the trigonocephaly did not seem to impact the matching process. Further differences could be caused by inaccuracy of the 3D-photo system or the CT-scan and its segmentation or registration.

In a growing skull, the CCFP could change and might require parametric correction to be able to perform sequential overlay of 3D photo data. This should be the subject of a follow-up study with CT-scans in different pediatric age groups. The $CCFP\sigma$ was only used for the method robustness test and was not further evaluated in the patient study. The $CCFP\sigma$ might give insight in the shape of the head as well as the effect of possible abnormalities of the head as suggested in the robustness test for the trigonocephaly and scaphocephaly shapes. This should be looked into and can potentially be used in clinical practice.

A final limitation of this study was the manual rotation used during the registration

process. This could result in small variation differences from patient to patient. An automated method to determine the rotations in these parts would be more objective and thus less vulnerable to these errors.

2.5. Conclusion

We have shown that the calculation of the CCFP is reliable and robust against deformations and missing data. Furthermore there is a considerable relative difference for the CCFP position in the synthetic shapes of the simulated trigonocephaly and scaphocephaly compared to the other shapes. This relative difference could potentially be used to quantify and/or qualify these conditions in CT-scans or 3D photos. Future research should be directed to investigate these features.

In the adult population, the CCFP-Skin and CCFP-Skull only differ a few millimeter in mean, 95% CI and standard deviation. Thus obtaining either of these values can be used to accurately estimate the other value. Since the difference of the CCFP-skin and CCFP-skull show few millimeter variations in individuals, the CCFP-skin can be used as an indication to where the sella turcica is located.

The CCFP-skull lies at average 1.9 *mm* more cranial and 1.4 *mm* more anterior than the CCFP-skin. The CCFP-skin is at (0.0, 27.1, 19.4) *mm* and the CCFP-skull at (-0.1, 28.9, 18.0) *mm* with a few-millimeter 95% CI, in relation to the sella turcica.

We have shown that the alignment of the skin surface of a 3D photo to a CT-scan while using the CCFP translation and manual rotation results in a near perfect match. We have shown a fit with an average sub millimeter difference in the first case and 2.3 *mm* difference in the second case which can be explained by growth and the use of a hairnet. In both cases there was a very small standard deviation for the difference (1.1 *mm*) suggesting that both cases were matched with equal accuracy. The hairnet in the 3D photo, and the missing data in the CT-scan had no observable impact on the CCFP calculation and matching. Hence the CCFP matching method is a viable option to match 3D photos with CT-scans. This could be done with sequential 3D photos as well, reducing the need for CT-scans and the radiation dose in the follow-up of cranial development.

In summary the CCFP method is a robust method for determining a position in the head by the skin surface or skull surface with a predictable position relative to the sella turcica. The CCFP of the skin and the skull have a known distance with a known variance relative to each other on which can be anticipated. Furthermore using the CCFP to overlay a 3D photo and CT-scan is a viable option that might also yield good results in sequential 3D photos. However more research is needed to fully explore the extent of the CCFP in cranial applications by itself

and in relation to other cranial measurement methods. Distinguishing between age and sex can give insight in the CCFP in the developing cranium. But most important is the potential to reduce the need for CT-scans, along with the radiation exposure in the follow-up of cranial development by using the CCFP.

2.6. Appendix

2.6.1. CCFP Calculation

The CCFP is calculated by determining the average of so called center points in a triangulated spherical object. Each face/triangle/polygon in the triangulated object has a center and a normal. Each center and normal can be considered as a skew line with the origin in the face center and the direction as the face normal. A so called center point can be calculated for each combination of skew lines that can be made. A center point is a point between two skew lines that has the closest and equal distance to two skew lines. For this the positions s and t on lines $L_n(s)$ and $L_m(t)$ are used to calculate the center point as shown in Ericson, Real-Time Collision Detection, 2005, (Chapter 5.1.8) [24]. An example of two skew lines and their center point is given in [Figure 2.6.1].

Averaging all skew line combinations for one given face gives the center-point (\mathbf{P}_{c,L_n}) for that face as can be seen in [Equation 2.6.1]. Only skew line combinations that have an absolute angle between each other larger than 30 degrees (and smaller than 330 degrees) will be used in the calculation. These cases will be add to the count of n_{f,L_n} as well. This is to exclude near-parallel face calculations that would result in outliers.

$$\mathbf{P}_{c,L_n} = \frac{1}{n_{f,L_n}} \sum \frac{L_n(s) + L_m(t)}{2} \quad (2.6.1)$$

Finally all center points are averaged to get the CCFP as can be seen in [Equation 2.6.2].

$$\text{CCFP} = \frac{1}{n_{faces}} \sum_{n=1}^{n_{faces}} \mathbf{P}_{c,L_n} \quad (2.6.2)$$

2.6.2. Calculation Software

Calculation of the CCFP is performed using Matlab 2014a (8.3) [20] with C++ and OpenCL 1.2 [22]. Matlab is used to calculate the skew lines of each polygon. The skew lines are send to a C++ library that facilitates OpenCL to calculate the center points. OpenCL was used to accelerate the calculation of the CCFP. In Matlab the CCFP σ and CCFP are calculated using

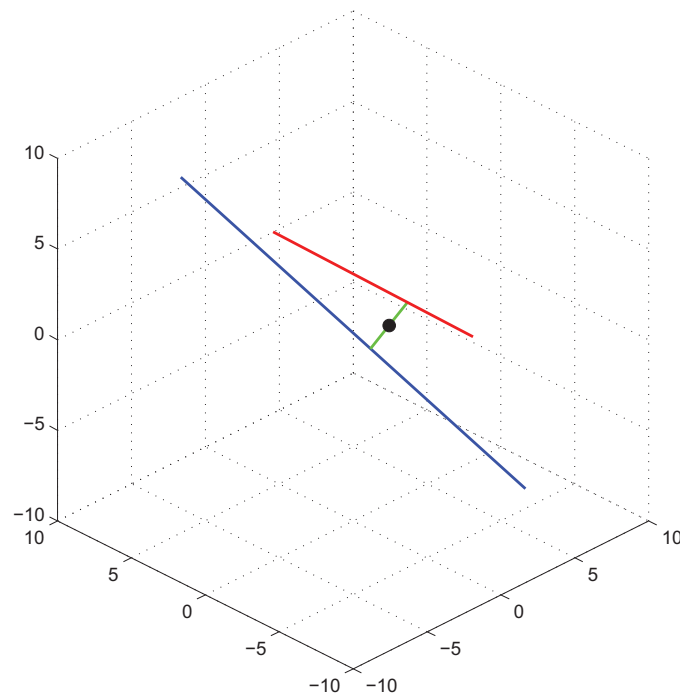


Figure 2.6.1: Example of two skew lines and the center point in 3D. A green line is drawn between two non-intersecting skew lines (red and blue) where the distance between these skew lines is shortest. The center of this green line is a center point. The distance from the center point to the each skew lines is equal.

the standard deviation and average of these center points. The software used was as proof of concept and thus the CCFP calculation is not limited to Matlab or C++. Other software (e.g. the free alternative Octave [25]) could be used to implement the CCFP calculation. Other acceleration techniques like CUDA [26] instead of OpenCL could also be used. Due to the simple math in the CCFP calculation completely stand-alone software could be written if desired.

References

- [20] The MathWorks Inc. "MATLAB and Statistics Toolbox Release 2014a". In: *Natick, Massachusetts, United States* (2014).
- [21] Tomas Möller and Ben Trumbore. "Fast, minimum storage ray/triangle intersection". In: *ACM SIGGRAPH 2005 Courses on - SIGGRAPH '05*. Vol. 2. 1. New York, New York, USA: ACM Press, 2005, p. 7. doi: 10.1145/1198555.1198746.

- [22] JE Stone, David Gohara, and Guochun Shi. "OpenCL: A parallel programming standard for heterogeneous computing systems". In: *Computing in science & engineering* (2010). DOI: 10.1109/MCSE.2010.69.
- [23] L Ibanez et al. *The ITK Software Guide*. Vol. Second. May. Kitware, Inc., 2005, p. 804. ISBN: 1930934157.
- [24] Christer Ericson. "Chapter 5 - Basic Primitive Tests". In: *Real-Time Collision Detection*. Ed. by Christer Ericson. The Morgan Kaufmann Series in Interactive 3D Technology. San Francisco: Morgan Kaufmann, 2005, pp. 125–233. ISBN: 978-1-55860-732-3. DOI: 10.1016/B978-1-55860-732-3.50010-3.
- [25] John W. Eaton. *GNU Octave*. URL: <http://www.gnu.org/software/octave/> (visited on 08/19/2015).
- [26] John Nickolls et al. "Scalable parallel programming with CUDA". In: *Queue* 6.2 (2008), p. 40. ISSN: 15427730. DOI: 10.1145/1365490.1365500.

3 | ISO-Surface Extraction for CCFP calculations

3.1. Introduction

CT-scans and other volume based imaging modalities use a set of voxels (3D pixel) to describe a volume. Certain computations executed on CT-scans are only possible or greatly benefit from vectorized surface data rather than voxel based data.

There are several methods of obtaining vectorized surface information from voxels; a process called (ISO-)surface extraction. ISO-surface extraction extracts a surface from a set of voxels where the voxel value equals a certain ISO-value. However there are differences between the ISO-surface extraction methods. This can for instance be the amount of details, the overall number of faces, the occurrence and amount of artifacts, the computation time.

The Computed Cranial Focal Point (CCFP) is a point in the cranium with a fixed position relative to the sella turcica that can be calculated based on such vectorized data [27]. This point can be calculated by using 3D models obtained from CT-scans or 3D Photos. The CCFP calculation uses surface normals and surface normal origins to determine the CCFP and its point-cloud.

The goal of this chapter is to perform a literature study to determine what the best ISO-surface algorithm is for the use in a CCFP computation pipeline. We look at the differences in the ISO-surface extraction methods regarding the numbers of faces, details, and artifacts of the mesh as well as the algorithms' computation times.

3.2. Criteria of ISO-surface algorithms

For the generation of the surface data for the CCFP computation there were several criteria. A hard criterium was the feasibility to implement the algorithm. If an algorithm for the given method is vaguely or not fully described it was excluded. One important aspect we took in

consideration is speed. With the current processing power there should be no need for long processing times. The amount of generated triangles was also of importance. More triangles describing the same surface usually accounts for more processing time in later steps. Another aspect to look at was the presence of artifacts and in what form they occurred.

Finally we looked if there were readily available implementations of the algorithm that could be integrated in Matlab 2015a (8.5) [28] with or without the use of C++.

3.3. History of ISO-surface algorithms

The oldest forms of (ISO-)surface extraction methods either focused on specific structures [29] or had known artifacts in the contour line implementation [30, 31].

A newer form of ISO surface extraction was the so called “Marching Cubes” (MC) algorithm (patented 1985-2005) [32]. MC uses look-up tables to define the set of triangles to be used as a replacement of a voxel. This was done by checking the ISO-values of neighboring voxels to choose an appropriate set of triangles from the look-up table. The use of look-up tables inspired another ISO-surface algorithm: “Marching Tetrahedra” [33] (MT). MT was a patent free alternative to MC with a different look-up table, triangle set and look-up method. Several suggested improvements on these algorithms have been made tackling specific per solution issues [34, 35, 36, 37, 38, 39].

A known property of the look-up table based algorithms was the inability to vary triangle size other than defined in the look-up table. This means that every triangle created would fit inside a voxel. As a result large flat surfaces that could easily be described with a few triangles are still described with at least as many triangles as there are voxels multiplied by the result of the look-up table. A single flat surface inside a voxel can hold up to 6 triangles in MC. A combination of both these properties can result in a very large amount of triangles for a single ISO-surface [40, 37, 41, 42].

In 1998 the surface nets method was introduced [43]. This is an iterative method that smooths out a cubic mesh based on the ISO-values to an optimum value for surface approximation. The issue with surface nets is that it is unable to produce sharp contours. A similar method called dual contouring was introduced to enable sharp corners [44]. As an addition it also includes a level of detail implementation based on octree simplification guided by quadric error functions.

Other algorithms and adaptations have been proposed that also reduce the amount of polygons while trying to maintain the shape of the model. An early example is the Splitting Box technique which converges a volume into increasingly smaller boxes for triangulation until a suitable quality is found [40]. Using a different look-up table and merging is an option to

reduce the triangle count as well [42]. Another early example utilizes merging and patching based on marching cubes and octree data [41]. Other forms combining MC with octree data are also known [45].

One of the latest known generations of ISO-surface algorithms are based on (surface) distribution algorithms of points or rays. The use of these algorithms require other techniques to acquire the point clouds. These can for instance be based on voronoi diagrams [46], on partial differential equations [47], or on least-squares projection [48]. Using the ISO-surface point cloud determination on a volume allows the use of techniques like interpolation, splines and quadrics to determine a more accurate and smooth point cloud. However these latest generations are more commonly used with point clouds acquired from laser scanners, IR based 3D cameras or similar rather than on volume datasets.

3.4. Selection of ISO-surface algorithms

The oldest techniques from the inventory are unsuitable due to not being suitable for true ISO-surface extraction.

The latest known generations are also unsuitable due to the use of additional point cloud generation techniques contributing in a large degree to the extraction time. For instance the least-squares projection technique takes from 21.3 to 36.8 seconds for a 75 thousand points point cloud in 2010 excluding the actual ISO-surface extraction itself [48]. Comparing this to a graphics processing unit (GPU) implementation using CUDA[26] MC algorithm of a magnetic resonance (MR) Brain results in processing from 10 to 305 million voxels per second in 2008 [49]. Although voxels and points in a point cloud are different objects in processing, comparing these speeds gives an idea of the difference in performance while trying to achieve a similar result; ISO-surface extraction.

So in essence the techniques to be further investigated are based on look-up tables (marching cubes or marching tetrahedra) and on interpolating methods (surface nets and dual contouring). All of these techniques so far have native or later implemented GPU implementations [49, 50, 51, 44, 52, 53] which is a good indication of fast processing.

MT is known to have an approximately four times higher triangle count compared to MC. Variations to reduce the amount of triangles using MT have been made [37]. However the GPU implementation is based on the original MT method [53]. Due to the high amount of triangles created (16 million is easily possible in a skull-ct) MT is no feasible option for now.

Surface nets usually yields a lower amount as MC. However surface nets have a build-in smoothing mechanism making them less suitable for sharp corners [51]. These sharp corners could occur in medical imaging. Hence surface nets is not used for the ISO-surface algorithm.

DC and surface nets have much in common. However dual contouring is able to represent sharp edges [54, 44, 51]. With the optional level of detail feature this is an interesting algorithm.

So in essence we have come to MC and DC as the final options. In the basic form both MC and DC have issues with non-manifold regions if two non-connected voxels are near. For both of these algorithms solutions have been proposed to fix these non-manifold regions [34, 54]. Furthermore in general DC produces less or an equal amount triangles than MC at the highest level of detail. Unfortunately the GPU implementations of both MC and DC do not have the non-manifold region fixes.

There is a small difference in quality for the GPU implementations of MC and DC. DC generally produces better quality meshes regarding the radii-ratio [51, 55].

Thus in the preference for the ISO-surface algorithm would be DC. Unfortunately there is no public GPU implementation of DC. Implementing the algorithm on the GPU from scratch was not a part of the scope of this study.

So in the end we will fall back on the OpenCL implementation of Marching Cubes as a second best. The algorithm, source code, and article [50] on this implementation are publicly available and thus our preferred choice.

3.5. Discussion

OpenCL Accelerated MC was our second best choice for ISO-surface extraction. DC is a promising measure with a higher quality however not readily available for implementation in Matlab 2015a. In future work we will look at the possibility for implementing DC in Matlab.

To date new ISO-surface algorithms are developed and older algorithms are updated to specifically target issues for certain applications. One of the main issues is the great number of available ISO-surface algorithms and the lack of systematic reviewing. Most articles will focus on just reviewing a single algorithm and comparing that towards other algorithms that they consider either standard, new, or otherwise relevant [35, 56, 51, 57]. This makes it difficult to properly select the ISO-surface algorithm that is best suited for a study or project.

Reviews of ISO-surface algorithms should have a set of standard test objects and outcome measures to objectively compare these algorithms. This should include a set of real-life or virtual volume objects with exact known shapes as well as a set of mathematically generated objects [56]. The real-life objects could e.g. be laser-scanned. These objects should cover scenario's for various fields of applications. This could include: sharp corners, round corners, flat surfaces, small gaps, big gaps, thin surfaces, thick surfaces. Outcome measures can be overall accuracy, flat surface accuracy, curvature accuracy, number of triangles, computation time, and others. Having standardized review would help to select the most suitable ISO-surface algorithm for a

study or project.

3.6. Conclusion

We reviewed a set of ISO-surface extraction algorithms to use on medical volume data. We looked into execution time, amount of generated triangles, accuracy, occurrence of artifacts and the availability of the algorithm for implementation in Matlab.

Our initial pick was Dual Countours based on the execution time, amount of triangles, and the accuracy. However there was no implementation with public source code available to implement in Matlab. Hence we choose for OpenCL accelerated Marching Cubes. With somewhat lesser accuracy and more triangles compared to DC this was our second choice based on the figures. However due to the availability we finally picked MC.

There are a large amount of other ISO-surface algorithms and the lack of standardized testing and evaluation made this review cumbersome to say the least. We reviewed the most common ISO-surface algorithms available. Many “exotic” ISO-surface algorithms were not reviewed for this study. We would like to suggest that ISO-surface algorithms in the future to be all tested in a similar fashion covering the most important aspects like computation time, triangle count, accuracy, artifacts, etc. This should greatly help to choose the ISO-surface algorithm best suited for a study or project in the future.

Furthermore we will look into dual contouring on the GPU in a generalized form for implementation in Matlab or similar software in future studies.

References

- [26] John Nickolls et al. “Scalable parallel programming with CUDA”. In: *Queue* 6.2 (2008), p. 40. ISSN: 15427730. DOI: 10.1145/1365490.1365500.
- [27] G. A. De Jong, T. J. J. Maal, and H. Delye. “The computed cranial focal point”. In: *Journal of Cranio-Maxillofacial Surgery* 43.9 (2015), pp. 1737–1742. ISSN: 18784119. DOI: 10.1016/j.jcms.2015.08.023.
- [28] United States Natick, Massachusetts. *Matlab 2015a*. Massachusetts, United States, 2015.
- [29] Christian Barillot et al. “3D Reconstruction of Cerebral Blood Vessels”. In: *IEEE Computer Graphics and Applications* 5.12 (1985), pp. 13–19. ISSN: 0272-1716. DOI: 10.1109/MCG.1985.276258.
- [30] H N Christiansen and T W Sederberg. “Conversion of Complex Contour Line Definitions Into Polygonal Element Mosaics”. In: *Computer Graphics* 12.3 (1978), pp. 187–192.

- [31] Larry Cook et al. "A Three-Dimensional Display System for Diagnostic Imaging Applications". In: *IEEE Computer Graphics and Applications* 3.5 (1983), pp. 13–19. ISSN: 0272-1716. DOI: 10.1109/MCG.1983.263180.
- [32] William E. Lorensen and Harvey E. Cline. "Marching cubes: A high resolution 3D surface construction algorithm". In: *ACM SIGGRAPH Computer Graphics* 21.4 (1987), pp. 163–169. ISSN: 00978930. DOI: 10.1145/37402.37422.
- [33] Jules Bloomenthal. "Polygonization of implicit surfaces". In: *Computer Aided Geometric Design* 5.4 (1988), pp. 341–355. ISSN: 01678396. DOI: 10.1016/0167-8396(88)90013-1.
- [34] Sundaresan Raman and Rephael Wenger. "Quality Isosurface Mesh Generation Using an Extended Marching Cubes Lookup Table". In: 27.3 (2008), pp. 3–10.
- [35] Paul Ning and Jules Bloomenthal. "Evaluation of implicit surface tilers". In: *IEEE Computer Graphics and Applications* 13.6 (1993), pp. 33–39. ISSN: 02721716. DOI: 10.1109/38.252552.
- [36] Samir Akkouché and Eric Galin. "Adaptive implicit surface polygonization using marching triangles". In: *Computer Graphics Forum* 20.2 (2001), pp. 67–80. ISSN: 01677055. DOI: 10.1111/1467-8659.00479.
- [37] G M Treece, R W Prager, and A H Gee. *Regularised marching tetrahedra: improving iso-surface extraction*. Tech. rep. CUED/F-INFENG/TR 333. 1998. DOI: [http://dx.doi.org/10.1016/S0097-8493\(99\)00076-X](http://dx.doi.org/10.1016/S0097-8493(99)00076-X).
- [38] Leif Kobbelt et al. "Feature Sensitive Surface Extraction from Volume Data". In: *Siggraph D* (2001), Pages: 57–66. DOI: 10.1145/383259.383265.
- [39] S.L. Chan and E.O. Purisima. "A new tetrahedral tessellation scheme for isosurface generation". In: *Computers & Graphics* 22.1 (1998), pp. 83–90. ISSN: 00978493. DOI: 10.1016/S0097-8493(97)00085-X.
- [40] Heinrich Müller and Michael Stark. "Adaptive generation of surfaces in volume data". In: *The Visual Computer* 9.4 (1993), pp. 182–199. ISSN: 01782789. DOI: 10.1007/BF01901723.
- [41] R. Shekhar et al. "Octree-based decimation of marching cubes surfaces". In: *Proceedings of Seventh Annual IEEE Visualization '96* (1996). DOI: 10.1109/VISUAL.1996.568127.
- [42] C. Montani, R. Scateni, and R. Scopigno. "Discretized Marching Cubes". In: *Proceedings Visualization '94* (1994). ISSN: 10702385. DOI: 10.1109/VISUAL.1994.346308.
- [43] Sff Gibson. "Constrained elastic surface nets: Generating smooth surfaces from binary segmented data". In: *Medical Image Computing and Computer-Assisted Intervention – MICCAI'98* (1998), pp. 888–898. ISSN: 16113349. DOI: 10.1007/BFb0056277.
- [44] Tao Ju et al. "Dual contouring of hermite data". In: *ACM Transactions on Graphics* 21.3 (2002), pp. 339–346. ISSN: 07300301. DOI: 10.1145/566654.566586.

- [45] Scott Schaefer and Joe Warren. "Dual marching cubes: Primal contouring of dual grids". In: *Computer Graphics Forum* 24.2 (2005), pp. 195–201. ISSN: 01677055. DOI: 10.1111/j.1467-8659.2005.00843.x.
- [46] M. Alliez, P. and Cohen-Steiner, D. and Tong, Y. and Desbrun. "Voronoi-based variational reconstruction of unoriented point sets". In: *Proceedings of the fifth Eurographics symposium on Geometry processing* (2007), pp. 39–48. ISSN: 17278384. DOI: 10.1145/1281991.1281997.
- [47] Paul Rosenthal and Lars Linsen. "Smooth surface extraction from unstructured point-based volume data using PDEs". In: *IEEE Transactions on Visualization and Computer Graphics* 14.6 (2008), pp. 1531–1538. ISSN: 10772626. DOI: 10.1109/TVCG.2008.164.
- [48] Dong Jin Yoo. "Rapid surface reconstruction from a point cloud using the least-squares projection". In: *International Journal of Precision Engineering and Manufacturing* 11.2 (2010), pp. 273–283. ISSN: 12298557. DOI: 10.1007/s12541-010-0031-2.
- [49] Christopher Dyken et al. "High-speed marching cubes using histopyramids". In: *Computer Graphics Forum* 27.8 (2008), pp. 2028–2039. ISSN: 01677055. DOI: 10.1111/j.1467-8659.2008.01182.x.
- [50] Erik Smistad, Anne C. Elster, and Frank Lindseth. "Real-Time Surface Extraction and Visualization of Medical Images using OpenCL and GPUs". In: *Nik-2012 november* (2012), pp. 141–152.
- [51] L. Schmitz et al. "Efficient and quality contouring algorithms on the GPU". In: *Computer Graphics Forum* 29.8 (2010), pp. 2569–2578. ISSN: 01677055. DOI: 10.1111/j.1467-8659.2010.01825.x.
- [52] ARM Limited. *Procedural modelling with geometry shaders*. URL: <https://malideveloper.arm.com/resources/sample-code/procedural-modelling-with-geometry-shaders/>.
- [53] Miłosz Ciznicki et al. "Efficient isosurface extraction using marching tetrahedra and histogram pyramids on multiple GPUs". In: *Lecture Notes in Computer Science (including subseries Lecture Notes in Artificial Intelligence and Lecture Notes in Bioinformatics)* 7204 LNCS.PART 2 (2012), pp. 343–352. ISSN: 03029743. DOI: 10.1007/978-3-642-31500-8_35.
- [54] Scott Schaefer, Tao Ju, and Joe Warren. "Manifold Dual Contouring". In: (), pp. 1–10.
- [55] C. A. Dietrich et al. "Edge transformations for improving mesh quality of marching cubes". In: *IEEE Transactions on Visualization and Computer Graphics* 15.1 (2009), pp. 150–159. ISSN: 10772626. DOI: 10.1109/TVCG.2008.60.
- [56] J. Patera and V. Skala. "A comparison of fundamental methods for iso surface extraction". In: *Machine Graphics and Vision* 13.4 (2004), pp. 329–343. ISSN: 12300535.

- [57] Timothy S. Newman and Hong Yi. “A survey of the marching cubes algorithm”. In: *Computers and Graphics (Pergamon)* 30.5 (2006), pp. 854–879. ISSN: 00978493. DOI: 10.1016/j.cag.2006.07.021.

4 | Real-Time Mesh Simplification Using Heterogeneous Computing

4.1. Confidential

The current chapter "Real-Time Mesh Simplification Using Heterogeneous Computing" is confidential, disclosed under NDA A16-0549.

The printed version of this thesis does not contain this chapter due to being confidential and disclosed under NDA A16-0549.

5 | Computed Cranial Focal Point in the Adult Population Revised

5.1. Introduction

The Computed Cranial Focal Point (CCFP) was introduced by *De Jong et al. (2015)* as a tool to assist head comparison based on soft-tissue from 3D Photos or CT-scans [27]. This method was improved by accounting for triangle size differences as could occur in 3D Photos or surfaces of CT-scans [Chapter 5.6.1]. Additional suggestions were made in the original article to further improve the calculation in the segmentation and registration process.

We aim for the best possible results and continuous improvement of the CCFP computation making it available for public use. Since we are aware that there were uncertainties in the original computation pipeline we decided to revise the original CCFP calculation pipeline.

Our goal of this chapter is to revise and optimize the original CCFP calculation pipeline for CT-scans. We look in depth in improving the segmentation, registration and simplification process. For longitudinal and grouped comparison we introduce sampling. We will test several levels of sampling where we will look at execution time, duplicate face samples and the CCFP positions relative to the sella turcica.

5.2. Materials and Methods

We revised the original CCFP calculation for CT-scans. We tested the revision on the original dataset of 36 adults [27]. We tackled some of the uncertainties that were introduced in the original method to make the computation more accurate. Furthermore we attempted to make the CCFP computation consistent for different degrees of detail for the mesh. The outline of the CCFP calculation pipeline used for CT-scans can be found in [Figure 5.2.1].

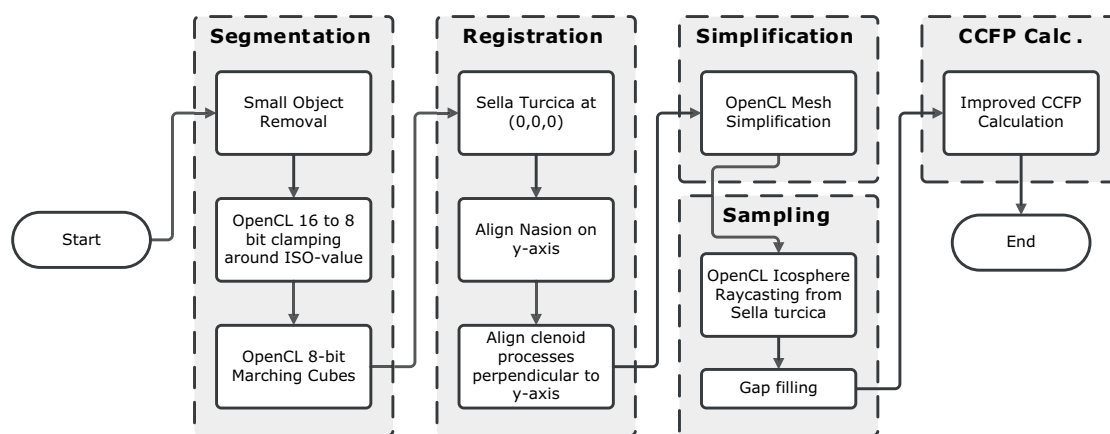


Figure 5.2.1: The revised CCFP calculation pipeline for CT-scans

5.2.1. Segmentation

We started with small object removal for objects with a Hounsfield unit (HU) of 167 and above. Objects not connected with a 18-connected neighborhood to the biggest object (skull) with a HU of 167 and above were removed. Segmentation was performed by a modified version of the OpenCL Marching Cubes (MC) implementation by *Smistad et al. (2012)* at an ISO-value of 167 HU [50]. The original implementation only accepted 8-bit volume data due to memory limitations while nearly all modern CT volume data uses 16-bit values storing the HU as signed 16-bit integers. Converting the volume by directly applying the threshold to have a binary image could result in jagged edges on the reconstruction. In order to overcome this issue we clamped the CT-scan in the range of -128 to 127 (signed 8 bit limit) with the threshold at 0 [Equation 5.2.1]. We subtracted the original threshold value and added 127 to every voxel value while clamping values <-128 to -128 and >127 to 127. This allowed 8-bit signed storage of the CT-scan in the range of the threshold. This is a lossless conversion regarding output mesh quality when compared to true 16-bit MC. Applying the MC algorithm on this new 8-bit dataset at an ISO-value of 0 resulted in a mesh with several millions of faces.

$$HU_{8bit,clamp} = clamp(HU_{16bit} - iso, -128, 127) \quad (5.2.1)$$

5.2.2. Registration

The registration procedure used is similar to that of *Tolhuisen et al. (2014)* [58]. Rotation and translation was established using a set of manually selected points. These points were the center of the sella turca, the left and right clinoid processes and the bony nasion. The rotation and translation matrices result in the sella turcia being placed at the origin (0,0,0) and the nasion on

the y-axis with the top of the skull in the z-direction. The clinoid processes are used to rotate the skull around the sella-nasion axis to place the midsagittal plane of the skull in the y-z plane. Manual rotational correction was applied if necessary due to the error in rotation caused by the natural variation in the clinoid processes [59, 60].

5.2.3. Mesh Simplification

Since a mesh with several million faces is impractical for the calculation time mesh simplification is an option. Furthermore in [Section 2] it is stated that we would require approximately 50.000 triangles for optimum computation time versus accuracy [27]. However this was based on some of the limitations that were in the original [Section 2]. Thus we used two levels of mesh simplification to reduce the number of triangles while maintaining the shape of the skull [See Section 4]. In this step we reduce the amount of triangles with 128-grid and 256-grid simplification. As a reference we also use no simplification at the cost of computation time.

5.2.4. Sampling

In order to further reduce the amount of triangles and explore a new optimum amount of triangles for computation we use sampling with an OpenCL implementation of raycasting [21]. Sampling is the technique of picking a (sub)set of datapoints from another set of datapoints or to approximate the original object. Since the original mesh is already sampled due to the simplification process we perform resampling to further reduce the number of data points. In our case the process of resampling allows to describe the surface as a set of datapoints of a reference shape. Raycasting is the technique of retrieving a data point from an intersection of a ray and a (triangulated) surface.

The resampling is done using raycasting [21] and a generated hemi-icosphere (half icosphere) as reference shape [61]. Each ray for sampling starts at the origin and crosses a vertex from the icosphere from where it can intersect with the registered and simplified CT-scan. Ray lengths of the intersection are stored and used to determine a new vertex point for resampling. We sample with different hemi-ico spheres with different numbers of vertices. We start at 91 samples up to 82241 samples.

A single triangle can be sampled multiple times by different rays depending on the size and position of the triangle as well as the direction and amount of rays. The amount of double samples indicate the usefulness of the sampling. In general the usefulnesses of the sampling decreases if the amount of double samples increase.

If there were missing vertices after sampling we used the average distance of the neighboring vertices to the origin to compute the new vertex position. This is done in a ring

by ring loop over 50 iterations to fill the small gaps. This was also execution with the aid of OpenCL.

5.2.5. Computed Cranial Focal Point Calculation

Although the mesh achieved from the sampling has relatively small deviations in face size compared to 3D Photos we still used the improved CCFP Calculation [Section 5.6.1]. This improved calculation compensates for face size differences that can occur in meshes. Using this method gives us the CCFP location per skull expressed as the relative position in *mm* as oriented in the sella-nasion orientation with midsaggital symmetry.

5.2.6. Hardware and Software

All calculations were performed using Matlab 2015a (8.5) [28] with C++ and OpenCL 1.2 [22]. OpenCL and C++ were used for the 16 to 8 bit clamping, the MC, mesh simplification, sampling and CCFP calculation.

All computations were executed on a Xeon E5 1620 v3 (3.5 Ghz) with 32 Gb RAM. As an OpenCL accelerator we used a GeForce GTX 970 with 4 Gb RAM.

5.2.7. Evaluation

For evaluation we compare the new CCFP value with the earlier reported CCFP value as found in the original study [27]. We further look into effect of the number of raycast samples on the mean CCFP, the σ of the CCFP, 95% CI, the amount of doubles as well as the computation time. For the computation time we look at the time for raycasting, gap filling and CCFP calculation.

5.3. Results

5.3.1. Segmentation, Registration, Simplification and Sampling

The small object removal worked similar as in the original CCFP study. There was no resampling of the volume data so there was no data loss prior to the ISO-surface/marching cubes. As a result a lower amount of HU threshold could be used for the segmentation to yield similar quality. The meshes obtained after marching cubes had a roughly 10-20 fold more triangles compared to the old method.

Registration in the original and new method were based on the sella turcica and the nasion. The difference between the two cases were the landmarks used for the midsaggital

alignment. In the original case the sphenoid base was used as a whole. It was visually observable that certain meshes showed a small lateral head tilt (roll) in the new method. This was corrected manually where visible.

The simplification correctly reduces the amount of triangles between 200.000 and 300.000 while maintaining the overall shape of the skull. As described in [Section ??] face inversion did occur occasionally. However since the sampling method can handle both inverted as non-inverted faces and thus this was not an issue. Smaller details like the sutures were no longer visible after the simplification as expected.

Sampling used a hemi-icosphere as raycast reference shape. The use of this shape minimizes any irregularities in sampling due to the uniform distribution of samples.

5.3.2. Calculated Computed Cranial Focal Point

The original results of the CCFP calculation can be found in [Table 5.3.4] [27]. The revised CCFP values with 128-grid simplification can be found in [Table 5.3.1], with 256-grid simplification can be found in [Table 5.3.2], and with no simplification can be found in [Table 5.3.3].

5.3.2.1. Effect of Simplification and Sampling

For lower numbers of samples there is at most a 0.1 *mm* difference in each direction between the mean CCFP that was either not simplified [Table 5.3.3], 128-grid simplified [Table 5.3.1] or 256-grid simplified [Table 5.3.2]. This effect goes up to 20641 point sampling.

The CCFP-x and CCFP-z values are respectively 1.6 ± 0.1 *mm* and 18.7 ± 0.1 *mm* for each degree of sampling and simplification except for the lowest sampling (91 points). However the CCFP-y value is less consistent. Up to 20641 point sampling there is only a ± 0.1 *mm* difference between each simplification degree again with the exception for the lowest sampling (91 points). For the two highest forms of sampling (46321 and 82241 points) there is a difference up to 0.6 *mm* between the observed CCFP-y values.

If we consider that no simplification at the highest number of samples for a CT-scan yields the most accurate result we can see that the CCFP value is (-1.6, 30.7, 18.6). Using a 3D Photo we would have a large degree of oversampling since the complete 3D photo would typically consist of a 50 to 80 fold less triangles compared to a CT-scan. The high number of triangles obtained via the CT-scans is due to the use of high resolution CT-scans (approximately 0.5 *mm*³ voxels). If we would have a lower resolution or simplification prior to the sampling we would automatically lose accuracy. Hence using the CCFP value of only the highest resolution CT-scans could result in inconsistency when comparing with lower quality CT-scans or 3D Photos.

Table 5.3.1: *The recalculated mean CCFP, standard deviation and 95% CI for the population of 36 patients for the skull in mm using various numbers of point samples with 128-grid simplification.*

| Samples | Mean (mm) | | | σ (mm) | | | 95% CI (mm) | | |
|---------|-----------|------|------|---------------|-----|-----|-------------|-------------|-------------|
| | x | y | z | x | y | z | x | y | z |
| 91 | -1,3 | 28,0 | 18,0 | 2,1 | 4,5 | 3,7 | -2,0 – -0,6 | 26,5 – 29,5 | 16,7 – 19,2 |
| 341 | -1,5 | 28,7 | 18,6 | 2,1 | 4,6 | 3,8 | -2,2 – -0,7 | 27,2 – 30,2 | 17,3 – 19,8 |
| 751 | -1,5 | 29,0 | 18,6 | 2,1 | 4,6 | 3,9 | -2,2 – -0,8 | 27,5 – 30,6 | 17,3 – 19,9 |
| 2941 | -1,6 | 29,4 | 18,7 | 2,1 | 4,7 | 3,9 | -2,3 – -0,9 | 27,8 – 31,0 | 17,4 – 20,0 |
| 5201 | -1,6 | 29,5 | 18,7 | 2,1 | 4,7 | 3,9 | -2,3 – -0,9 | 28,0 – 31,1 | 17,4 – 20,0 |
| 11641 | -1,6 | 29,7 | 18,7 | 2,1 | 4,8 | 3,9 | -2,3 – -0,9 | 28,1 – 31,3 | 17,4 – 20,1 |
| 20641 | -1,6 | 29,8 | 18,8 | 2,1 | 4,8 | 4,0 | -2,3 – -0,9 | 28,2 – 31,4 | 17,4 – 20,1 |
| 46321 | -1,6 | 30,0 | 18,8 | 2,1 | 4,8 | 4,0 | -2,3 – -0,9 | 28,4 – 31,6 | 17,4 – 20,1 |
| 82241 | -1,6 | 30,1 | 18,8 | 2,1 | 4,8 | 4,0 | -2,2 – -0,9 | 28,5 – 31,7 | 17,4 – 20,1 |

Table 5.3.2: *The recalculated mean CCFP, standard deviation and 95% CI for the population of 36 patients for the skull in mm using various numbers of point samples with 256-grid simplification.*

| Samples | Mean (mm) | | | σ (mm) | | | 95% CI (mm) | | |
|---------|-----------|------|------|---------------|-----|-----|-------------|-------------|-------------|
| | x | y | z | x | y | z | x | y | z |
| 91 | -1,3 | 28,0 | 18,0 | 2,1 | 4,5 | 3,7 | -2,0 – -0,6 | 26,5 – 29,5 | 16,7 – 19,2 |
| 341 | -1,5 | 28,7 | 18,6 | 2,1 | 4,6 | 3,8 | -2,2 – -0,8 | 27,2 – 30,2 | 17,3 – 19,8 |
| 751 | -1,5 | 29,0 | 18,6 | 2,1 | 4,6 | 3,9 | -2,2 – -0,8 | 27,5 – 30,5 | 17,3 – 19,9 |
| 2941 | -1,6 | 29,4 | 18,7 | 2,1 | 4,7 | 3,9 | -2,3 – -0,9 | 27,8 – 31,0 | 17,4 – 20,0 |
| 5201 | -1,6 | 29,6 | 18,7 | 2,1 | 4,7 | 3,9 | -2,3 – -0,9 | 28,0 – 31,1 | 17,4 – 20,0 |
| 11641 | -1,6 | 29,7 | 18,7 | 2,1 | 4,8 | 3,9 | -2,3 – -0,9 | 28,1 – 31,3 | 17,4 – 20,1 |
| 20641 | -1,6 | 29,9 | 18,8 | 2,1 | 4,8 | 3,9 | -2,3 – -0,9 | 28,3 – 31,5 | 17,4 – 20,1 |
| 46321 | -1,6 | 30,2 | 18,7 | 2,0 | 4,8 | 4,0 | -2,2 – -0,9 | 28,6 – 31,8 | 17,4 – 20,1 |
| 82241 | -1,6 | 30,5 | 18,7 | 2,1 | 4,7 | 4,0 | -2,2 – -0,9 | 28,9 – 32,1 | 17,4 – 20,0 |

Table 5.3.3: *The recalculated mean CCFP, standard deviation and 95% CI for the population of 36 patients for the skull in mm using various numbers of point samples without simplification.*

| Samples | Mean (mm) | | | σ (mm) | | | 95% CI (mm) | | |
|---------|-----------|------|------|---------------|-----|-----|-------------|-------------|-------------|
| | x | y | z | x | y | z | x | y | z |
| 91 | -1,3 | 28,0 | 18,0 | 2,1 | 4,5 | 3,7 | -2,0 – -0,6 | 26,5 – 29,5 | 16,7 – 19,2 |
| 341 | -1,5 | 28,7 | 18,6 | 2,1 | 4,6 | 3,8 | -2,2 – -0,8 | 27,2 – 30,2 | 17,3 – 19,8 |
| 751 | -1,5 | 29,0 | 18,6 | 2,1 | 4,6 | 3,9 | -2,2 – -0,8 | 27,5 – 30,5 | 17,3 – 19,9 |
| 2941 | -1,6 | 29,4 | 18,7 | 2,1 | 4,7 | 3,9 | -2,3 – -0,9 | 27,8 – 31,0 | 17,4 – 20,0 |
| 5201 | -1,6 | 29,6 | 18,7 | 2,1 | 4,7 | 3,9 | -2,3 – -0,9 | 28,0 – 31,2 | 17,4 – 20,0 |
| 11641 | -1,6 | 29,8 | 18,7 | 2,1 | 4,8 | 3,9 | -2,2 – -0,9 | 28,2 – 31,3 | 17,4 – 20,1 |
| 20641 | -1,6 | 29,9 | 18,7 | 2,1 | 4,8 | 4,0 | -2,2 – -0,9 | 28,3 – 31,5 | 17,4 – 20,1 |
| 46321 | -1,6 | 30,3 | 18,7 | 2,1 | 4,7 | 4,0 | -2,2 – -0,9 | 28,7 – 31,9 | 17,4 – 20,0 |
| 82241 | -1,5 | 30,7 | 18,6 | 2,0 | 4,7 | 4,0 | -2,2 – -0,9 | 29,2 – 32,3 | 17,3 – 20,0 |

Table 5.3.4: *The original mean CCFP, standard deviation and 95% CI for the population of 36 patients for the skull in mm.*

| CCFP | Mean (mm) | σ | 95%CI |
|--------------------|-----------|----------|-------------|
| Skull _x | 0.0 | 0.5 | -0.3 – 0.1 |
| Skull _y | 29.9 | 4.6 | 28.3 – 31.5 |
| Skull _z | 18.6 | 4.2 | 17.2 – 20.0 |

An effect of higher sampling is oversampling. Oversampling can result in a mesh consisting of more triangles than the original mesh that was sampled. The effect of oversampling can best be illustrated through the number of duplicate face samples. In [Tables 5.3.5, 5.3.6, 5.3.7] the number and percentage of double samples is shown for each number of samples taken respectively for 128-grid, 256-grid and no simplification. Independent of the prior simplification there is only a small difference in double samples up to 5201 sampling. For 11641 and above there is an increasing difference in double samples between the levels of simplification varying from 1.0% to 40.8 %. The effect of the double samples on the CCFP position is limited as can be seen in [Tables 5.3.1, 5.3.2, 5.3.3]. As said earlier, up to 20641 samples there is a ± 0.1 mm difference between each simplification degree. For the current dataset this yields 6.6%, 1.5% and 1.0 % double samples for respectively 128-grid, 256-grid and no sampling.

Table 5.3.5: *The timing and double samples per sampling after raycasting using 128-grid simplification.*

| Samples | Timing (s) | | | | Double samples | |
|---------|------------|----------|------|-------|----------------|------|
| | Raycast | Gap fill | CCFP | Total | (#) | (%) |
| 91 | 0.37 | 0.18 | 0.19 | 0.74 | 2 | 2.2 |
| 341 | 0.38 | 0.18 | 0.19 | 0.74 | 5 | 1.5 |
| 751 | 0.37 | 0.17 | 0.18 | 0.72 | 11 | 1.5 |
| 2941 | 0.38 | 0.19 | 0.19 | 0.75 | 37 | 1.3 |
| 5201 | 0.38 | 0.20 | 0.20 | 0.79 | 70 | 1.3 |
| 11641 | 0.38 | 0.22 | 0.21 | 0.82 | 304 | 2.6 |
| 20641 | 0.46 | 0.31 | 0.27 | 1.04 | 1361 | 6.6 |
| 46321 | 0.87 | 0.71 | 0.53 | 2.11 | 10392 | 22.4 |
| 82241 | 1.45 | 1.68 | 1.26 | 4.39 | 33520 | 40.8 |

Table 5.3.6: *The timing and double samples per sampling after raycasting using 256-grid simplification.*

| Samples | Timing (s) | | | | Double samples | |
|---------|------------|----------|------|-------|----------------|-----|
| | Raycast | Gap fill | CCFP | Total | (#) | (%) |
| 91 | 0.90 | 0.19 | 0.19 | 1.28 | 2 | 2.2 |
| 341 | 0.91 | 0.19 | 0.20 | 1.29 | 5 | 1.5 |
| 751 | 0.88 | 0.18 | 0.19 | 1.25 | 10 | 1.3 |
| 2941 | 0.90 | 0.19 | 0.19 | 1.28 | 35 | 1.2 |
| 5201 | 0.91 | 0.20 | 0.20 | 1.30 | 60 | 1.2 |
| 11641 | 0.95 | 0.23 | 0.23 | 1.42 | 138 | 1.2 |
| 20641 | 1.23 | 0.31 | 0.26 | 1.81 | 306 | 1.5 |
| 46321 | 2.68 | 0.72 | 0.51 | 3.91 | 1674 | 3.6 |
| 82241 | 4.68 | 1.66 | 1.24 | 7.58 | 7434 | 9.0 |

Table 5.3.7: *The timing and double samples per sampling after raycasting using no simplification.*

| Samples | Timing (s) | | | | Double samples | |
|---------|------------|----------|------|-------|----------------|-----|
| | Raycast | Gap fill | CCFP | Total | (#) | (%) |
| 91 | 3.15 | 0.16 | 0.17 | 3.49 | 2 | 2.2 |
| 341 | 3.16 | 0.16 | 0.17 | 3.49 | 5 | 1.5 |
| 751 | 3.10 | 0.16 | 0.16 | 3.43 | 10 | 1.3 |
| 2941 | 3.11 | 0.16 | 0.16 | 3.43 | 35 | 1.2 |
| 5201 | 3.36 | 0.18 | 0.18 | 3.72 | 59 | 1.1 |
| 11641 | 3.41 | 0.19 | 0.18 | 3.77 | 125 | 1.1 |
| 20641 | 4.03 | 0.29 | 0.25 | 4.57 | 216 | 1.0 |
| 46321 | 9.13 | 0.71 | 0.50 | 10.34 | 483 | 1.0 |
| 82241 | 16.52 | 1.68 | 1.19 | 19.39 | 1043 | 1.3 |

Finally there is computation time. We measured the most computational intensive tasks (Raycasting, Gap filling, CCFP calculation) for each number of sampling per simplification [Tables 5.3.5,5.3.6,5.3.7]. The simplification process in all cases was below 100 *ms* and therefore not reported. The total execution time for the 128-grid simplification is below one second up to 11641 samples. At 20641 samples this is just above one second. For 46321 and 82241 samples this is respectively 2.11 and 4.39 seconds. The 256-grid simplification starts at 1.28 seconds and increases to 1.81 seconds at 20641 samples. Again a bigger increase in computation time can be seen for the highest two forms of sampling up to 7.58 seconds. Using no simplification results in a 3.49 second execution time at the lowest sampling up to 19.39 seconds for the highest sampling. The primary cause for the increased execution time is the raycasting. Logically both the gap fill and CCFP computation show similar execution times for each form of sampling regardless of prior simplification due to processing the same amount of data.

Regarding consistency in CCFP position, double samples and timing we found that either 11641 or 20641 samples is the optimum number for the CCFP computation. This results in a fast and consistent computation of the CCFP for both lower and higher detailed 3D models.

5.4. Discussion

5.4.1. CCFP result difference

There are some small differences between the positions from the old and new CCFP calculations. The two most prominent differences are in the x-direction at -1.6 mm and in the y-direction 1.0 mm . Those changes can be explained by certain steps in the new CCFP calculation methods. When evaluating the results we saw that there was a certain degree of lateral head tilt. Assuming that in a symmetrical skull the x-value of the CCFP should be at 0 mm we can explain offsets of the x-value by head tilt. Furthermore there is a specific order in which the clinoid processes are selected (right side first) could give a small bias of selecting the left clinoid process by referring to the right process.

The offset in the y-direction is most likely due to a better calculation. In the original article head flexion in the CT-scan was given as a cause for incomplete data due to the volume selection. Since we are no longer using volume selection but surface selection with sampling we no longer have this issue. This means that the current method has an optimal surface for the CCFP calculation. Hence this is most likely the cause for the 1.0 mm offset in the y-direction compared to the original.

5.4.2. New CCFP Calculation Method

The new method was performed in 5 main steps: Segmentation, Registration, Simplification, Sampling and CCFP calculation. We saw that the visible lateral head tilt could occur during this new method.

There is a certain degree of anatomical variation in the anterior clinoid process at either the left, right or both sides. For instance in 2015 the occurrence of a carotid-clinoid foramen and sella turcica bridge was found in 14.2 % and 14.4 % of in 597 ct-scans [59]. Other figures have been reported throughout time ranging from 6.27% to 36.00 % (with own findings at 16.75%) for the carotid-clinoid foramen [60]. The same study reports the occurrence of interclinoid bone bridges between 3.04% and 8.68% (with own findings at 6.75%). This could make harder to consistently select the most posterior position of the anterior clinoid process. This could result in lateral head tilt issues when trying to select the clinoid processes in registration.

The registration could be automated. Semi-automatic registration has been described by manually picking landmarks that are automatically refined for orientation [62]. Recent articles focusing on the automatic registration of the Frankfurt plane and midsagittal plane without the use of symmetry planes [63, 64]. The latter articles are unclear on the landmark detection

algorithm, but there should be no issues in implementing one of the many possible landmark detection options [65, 66]. These methods could be used as a replacement for (semi-) automatic registration.

Other aspects of the calculation method were swift, of good quality and without any issues.

5.5. Conclusion

We revised the CCFP calculation method with a new pipeline of steps to calculate the CCFP from CT-scans. The results of this method showed little difference with the original CCFP calculation method. The differences can be explained by the various steps taken in the new process. The less favorable difference (x-direction) can be overcome by reverting to the old registration method, using different landmarks, or changing to automatic registration. The y-direction difference in the new calculation is thought to be better than the original and can be explained by a more optimum surface for the calculation.

Overall the CCFP calculation was improved over the original method and should be considered the new standard in CCFP calculations for CT-scans using 11641 or 20641 samples in the resampling process.

5.6. Appendix

5.6.1. Improving the CCFP Calculation

The improved CCFP calculation adds a correction for triangle size. Triangle sizes in a 3D photo can typically vary up to 50x larger to 20x smaller than the mean triangle size [Figure 5.6.1]. This can result in less accurate CCFP calculations since larger triangles have an equal influence as smaller triangles. This makes the accuracy prone to the sampling resolution and 3d reconstruction. In order to compensate for this effect there is a weight factor for the triangle size implemented in the CCFP calculation.

5.6.1.1. Original CCFP Calculation

In the original CCFP is calculated by determining and averaging the center points in a triangulated spherical object [27]. In the original article two properties of a triangle are used: the normal and the center. A skew line is determined by using the normal and a center of a triangle. The original center point calculation for a given triangle is described in [Equation 5.6.1].

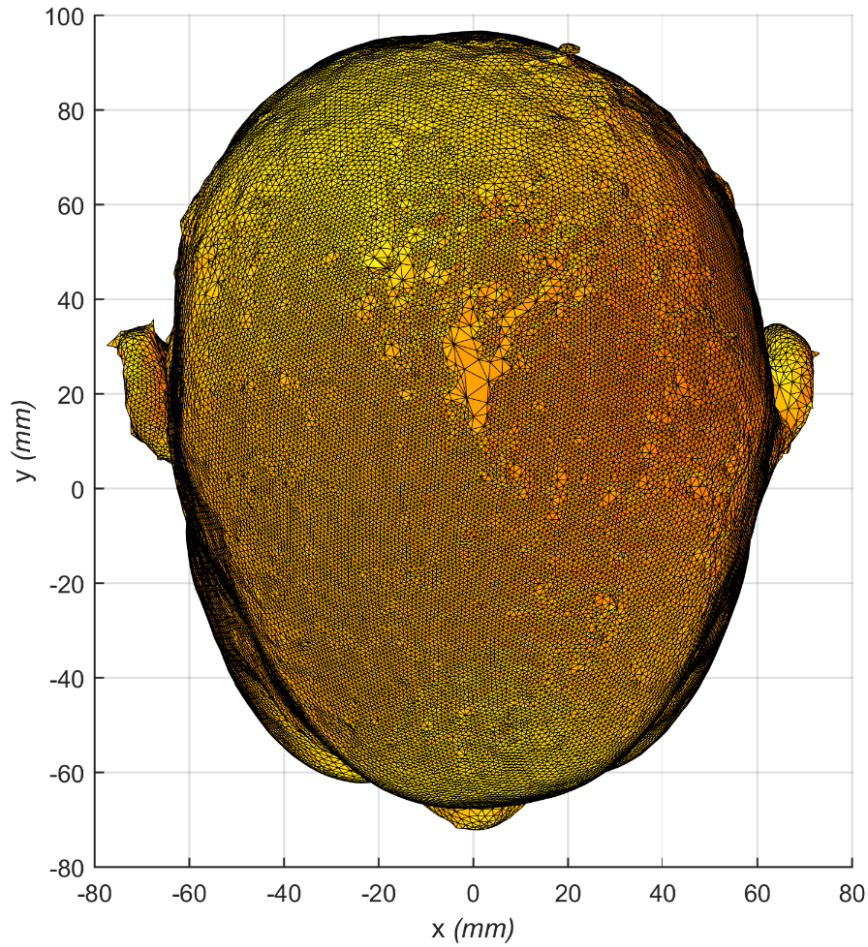


Figure 5.6.1: Triangle size difference in a 3D Photo.

The center point \mathbf{P}_{c,L_n} is determined by the position of s and t on the skew lines $L_n(s)$ and $L_m(t)$ where the distance between these skew lines is minimal. The skew line $L_n(s)$ is the line of the triangle of which the center point is determined. The skew lines $L_m(t)$ are the lines that can form a pair with $L_n(s)$. A pair can be formed if there is absolute angle larger than 30 degrees and smaller than 330 degrees between the two skew lines. The total is divided by the amount of formed pairs n_{f,L_n} .

$$\mathbf{P}_{c,L_n} = \frac{1}{n_{f,L_n}} \sum \frac{L_n(s) + L_m(t)}{2} \quad (5.6.1)$$

As a final step all center points are averaged to determine the CCFP [Equation 5.6.2].

$$\text{CCFP} = \frac{1}{n_{faces}} \sum_{n=1}^{n_{faces}} \mathbf{P}_{c,L_n} \quad (5.6.2)$$

5.6.1.2. Improved CCFP Calculation

The first step of the improvement calculation is in the center point calculation. In this calculation we consider the surface area of the paired triangles as a weighting factor for the center point. For this we use the surface area (A_m) of each triangle of which skew line can be used as a pair. In this version we multiply the surface area per sub-center point and later on divide the sum of these sub-center points by the sum of the surface area of the triangles that can be used as a pair. This results in the new [Equation 5.6.3] where the effect of the size of the paired triangles is taken in consideration.

$$\mathbf{P}_{c,L_n} = \frac{1}{\sum A_m} \sum A_m \frac{L_n(s) + L_m(t)}{2} \quad (5.6.3)$$

The second step of the improvement is in the averaging calculation. Here we take the effect of the size of the triangle of the center point on the CCFP itself. This is done by multiplying the surface area (A_n). per center point and dividing the total with the sum of the surface area as seen in [Equation 5.6.4].

$$\mathbf{CCFP} = \frac{1}{\sum A_n} \sum_{n=1}^{n_{faces}} \mathbf{P}_{c,L_n} A_n \quad (5.6.4)$$

References

- [21] Tomas Möller and Ben Trumbore. “Fast, minimum storage ray/triangle intersection”. In: *ACM SIGGRAPH 2005 Courses on - SIGGRAPH '05*. Vol. 2. 1. New York, New York, USA: ACM Press, 2005, p. 7. doi: 10.1145/1198555.1198746.
- [22] JE Stone, David Gohara, and Guochun Shi. “OpenCL: A parallel programming standard for heterogeneous computing systems”. In: *Computing in science & engineering* (2010). doi: 10.1109/MCSE.2010.69.
- [27] G. A. De Jong, T. J. J. Maal, and H. Delye. “The computed cranial focal point”. In: *Journal of Cranio-Maxillofacial Surgery* 43.9 (2015), pp. 1737–1742. issn: 18784119. doi: 10.1016/j.jcms.2015.08.023.
- [28] United States Natick, Massachusetts. *Matlab 2015a*. Massachusetts, United States, 2015.
- [50] Erik Smistad, Anne C. Elster, and Frank Lindseth. “Real-Time Surface Extraction and Visualization of Medical Images using OpenCL and GPUs”. In: *Nik-2012 november* (2012), pp. 141–152.

- [58] M L Tolhuisen et al. "A Method for the Creation of Normative Paediatric Skull Models : A Pilot Study". In: *International Journal of Engineering Science and Innovative Technology* 3.6 (2014), pp. 1–7.
- [59] Marcos Devanir Silva da Costa et al. "Anatomical Variations of the Anterior Clinoid Process". In: *Operative Neurosurgery* 0.0 (2015), p. 1. ISSN: 2332-4252. DOI: 10.1227/NEU.0000000000001138.
- [60] Eldan Kapur and Amina Mehić. "Anatomical variations and morphometric study of the optic strut and the anterior clinoid process". In: *Bosnian Journal of Basic Medical Sciences* 12.2 (2012), pp. 88–93. ISSN: 15128601.
- [61] Dave Shreiner, Mason Woo, and Tom Davis. *OpenGL Programming Guide: The Official Guide to Learning OpenGL, Version 2*. 5th. 2006, p. 896. ISBN: ISBN 0-321-33573-2.
- [62] Cauter Van Sofie et al. "3D cephalometry: A new approach for landmark identification and image orientation". In: *IFMBE Proceedings*. Vol. 22. 2008, pp. 1442–1445. ISBN: 9783540892076. DOI: 10.1007/978-3-540-89208-3_342.
- [63] Kun Zhang, Yuan Cheng, and Wee Kheng Leow. "Dense correspondence of skull models by automatic detection of anatomical landmarks". In: *Lecture Notes in Computer Science (including subseries Lecture Notes in Artificial Intelligence and Lecture Notes in Bioinformatics)* 8047 LNCS.PART 1 (2013), pp. 229–236. ISSN: 03029743. DOI: 10.1007/978-3-642-40261-6_27.
- [64] Yuan Cheng, Wee Kheng Leow, and Thiam Chye Lim. "Automatic identification of Frankfurt plane and mid-sagittal plane of skull". In: *Proceedings of IEEE Workshop on Applications of Computer Vision* (2012), pp. 233–238. ISSN: 21583978. DOI: 10.1109/WACV.2012.6162994.
- [65] Silvio Filipe and LuĂás A. Alexandre. "A comparative Evaluation of 3D keypoint detectors". In: (2013), pp. 145–148.
- [66] Federico Tombari, Samuele Salti, and Luigi Di Stefano. "Performance evaluation of 3D keypoint detectors". In: *International Journal of Computer Vision* 102.1-3 (2013), pp. 198–220. ISSN: 09205691. DOI: 10.1007/s11263-012-0545-4.

6 | Computed Cranial Focal Point Evolution in a Normal Pediatric Population

6.1. Introduction

Craniosynostosis is a condition in which one or more of the cranial sutures fuse prematurely. The incidence of this condition is estimated at 1 in 2000 to 1 in 2500 live births [1]. Objective monitoring of the effects of craniosynostosis surgery and its follow up interventions is performed with the use of skull growth measurement. Especially the use of 3D measurements has become more popular in the past years. However most of these utilize CT-scans which result in a potentially harmful ionizing radiation for the patient if these would be applied in a clinical setting [11].

Stereo photogrammetry is a new radiation free 3D measurement tool for monitoring skull growth after surgical craniosynostosis interventions [14]. A common reference point for skull comparison is the sella turcica since its relative position is assumed to be more or less stable during skull growth [19]. However this point can not be determined directly using stereo photogrammetry. A new method to determine a similar reference point, the computed cranial focal point (CCFP), was proposed using a 3D surface from a 3D Photo [27]. The CCFP has a fixed location relative to the sella turcica. This allows orienting a head in the sella turcica-nasion plane anchored to the sella turcica for longitudinal follow-up. Using this method it is possible to perform radiation-free evaluations for either longitudinal follow-up of a single patient as well as to evaluate groups of patients. This further allows for averaging groups of patients to be compared.

However the study by *De Jong (2015)* did not incorporate the effect of the growing cranium on the CCFP position of pediatric patients. In a perfect scenario the CCFP position would remain constant during cranium development. This would allow direct sequential 3D photo overlaying. It is more likely though that the position changes over time in the developing cranium. If the position over time is known or can be calculated with e.g. interpolation models,

3D photo to 3D photo overlaying can be preformed. Thus a study to map the position of the CCFP in these skulls is required.

The goal of the study is to describe the morphology of the CCFP in the aging pediatric skull based on CT-scans.

6.2. Materials and Methods

In order to determine the path the CCFP follows over time in pediatric patients without introducing a potentially harmful radiation dose, a retrospective study is chosen. CT-scans of pediatric patients were selected and the CCFP calculation performed. Statistical analysis on the found CCFP points is applied in order to validate if the CCFP points can be used to determine a certain path.

6.2.1. Patient Study Scan selection

For this study scans were selected from pediatric patients that came to Radboud UMC and underwent a cranial CT-scan in the past year. The patient were not allowed to have any form of trauma or pathologies of the cranium or the surrounding skin. The patient group started with 86 pediatric patients of which 30 were excluded due to data and segmentation problems. The final group consists of 56 pediatric patients age 0 to 50 months of which 34 were male. The average age of both the male and female patients was 18 months. All of the scans were anonymized conform the institution's policy. The scans were made with various CT-scanners of which the majority was scanned using a pixel spacing of $0.43 \times 0.43 \text{ mm}$ and a slice thickness of 0.5 mm .

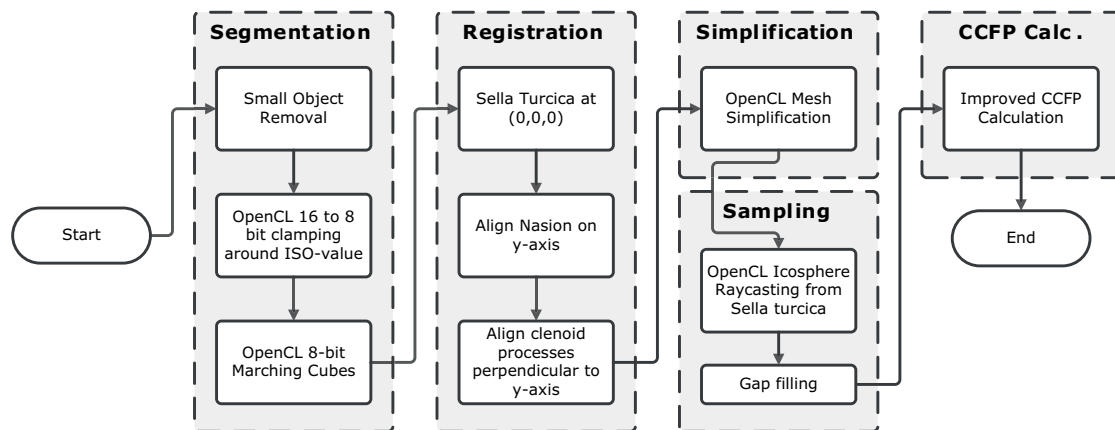
The patients were divided in the following age groups: 0–1, 2–4, 5–7, 8–10, 11–14, 15–18, 19–24, 25–36, 37–50 months. The age per patient was rounded to the nearest month. The final distribution of patients can be found in [Table 6.2.1].

Table 6.2.1: *The distribution of pediatric patients per age group and sex.*

| Age (months) | Male | Female | Total |
|--------------|------|--------|-------|
| 0-1 | 1 | 2 | 3 |
| 2-4 | 3 | 3 | 6 |
| 5-7 | 3 | 0 | 3 |
| 8-10 | 4 | 0 | 4 |
| 11-14 | 4 | 7 | 11 |
| 15-18 | 6 | 2 | 8 |
| 19-24 | 5 | 3 | 8 |
| 25-36 | 4 | 1 | 5 |
| 37-50 | 4 | 4 | 8 |

6.2.2. Segmentation, Registration, Sampling

For the segmentation, registration and sampling we use the same steps as in the CCFP calculation pipeline as in [Section 5]. The outline of the CCFP calculation pipeline is shown in [Figure 6.2.1].

**Figure 6.2.1:** *The revised CCFP calculation pipeline for CT-scans*

To compensate for the collagen rich bone in these pediatric population we varied the threshold around 167 HU for optimum results. We further used a 20641 point hemi-icosphere for sampling.

6.2.3. CCFP Calculation

The improved CCFP computation was used similar as in [Section 5]. This improved CCFP computation [Section 5.6.1 takes triangle size differences into account. These triangle difference can occur in marching cubes.

6.2.4. Statistical analysis

We compared the means of the CCFP in each direction of the patients per group for the total volume and anterior volume to determine if there is a significant difference. We start with a Shapiro-Wilks Test to test for normality. We also performed a Levene's Test to test the Homogeneity of Variances. We further executed a ANOVA test and alternatively a Brown Forsythe and Welch Test and of if the homogeneity of variances was not met. Lastly we used a Games-Howell Post-hoc test to determine which means were significantly different from the other groups ($\alpha = 0.05$).

6.3. Results

The results of the mean CCFP, the standard deviation of the CCFP and the 95% CI of the CCFP per age group is shown for the skull [Table 6.3.1].

Table 6.3.1: *The mean CCFP, Standard deviation of the CCFP and the 95% CI for the skull in each direction for the pediatric patients ordered by age group.*

| Age (months) | n | Mean CCFP (mm) | | | STD. CCFP (mm) | | | 95% CI (mm) | | |
|-----------------|----|----------------|------|------|----------------|------------|------------|-------------|-----------|-----------|
| | | X | Y | Z | σ_x | σ_y | σ_z | X | Y | Z |
| 0-1 | 3 | -1.5 | 25.2 | 12.3 | 1.6 | 1.8 | 1.6 | -5.4-2.3 | 20.8-29.5 | 16.2-8.4 |
| 2-4 | 6 | -0.3 | 30.7 | 17.0 | 1.9 | 2.5 | 4.4 | -2.3-1.7 | 28.1-33.3 | 21.6-12.4 |
| 5-7 | 3 | -1.0 | 33.9 | 13.3 | 0.3 | 2.3 | 1.5 | -1.8- -0.2 | 28.3-39.5 | 17.2-9.5 |
| 8-10 | 4 | -0.7 | 34.1 | 12.4 | 0.9 | 1.9 | 3.4 | -2.1-0.7 | 31.1-37.2 | 17.7-7.0 |
| 11-14 | 11 | -0.4 | 33.9 | 13.9 | 1.2 | 1.4 | 3.8 | -1.2-0.4 | 32.9-34.8 | 16.4-11.4 |
| 15-18 | 8 | -0.4 | 33.4 | 17.0 | 1.3 | 4.6 | 3.1 | -1.5-0.7 | 29.5-37.2 | 19.6-14.5 |
| 19-24 | 8 | 0.0 | 33.9 | 16.4 | 2.2 | 3.8 | 1.5 | -1.9-1.8 | 30.7-37.1 | 17.7-15.1 |
| 25-36 | 5 | -0.6 | 35.6 | 17.9 | 1.5 | 4.7 | 5.9 | -2.4-1.3 | 29.7-41.5 | 25.2-10.7 |
| 37-50 | 8 | -0.9 | 33.9 | 17.7 | 0.8 | 2.9 | 2.4 | -1.5- -0.2 | 31.4-36.3 | 19.7-15.7 |

6.3.1. Trend interpretation

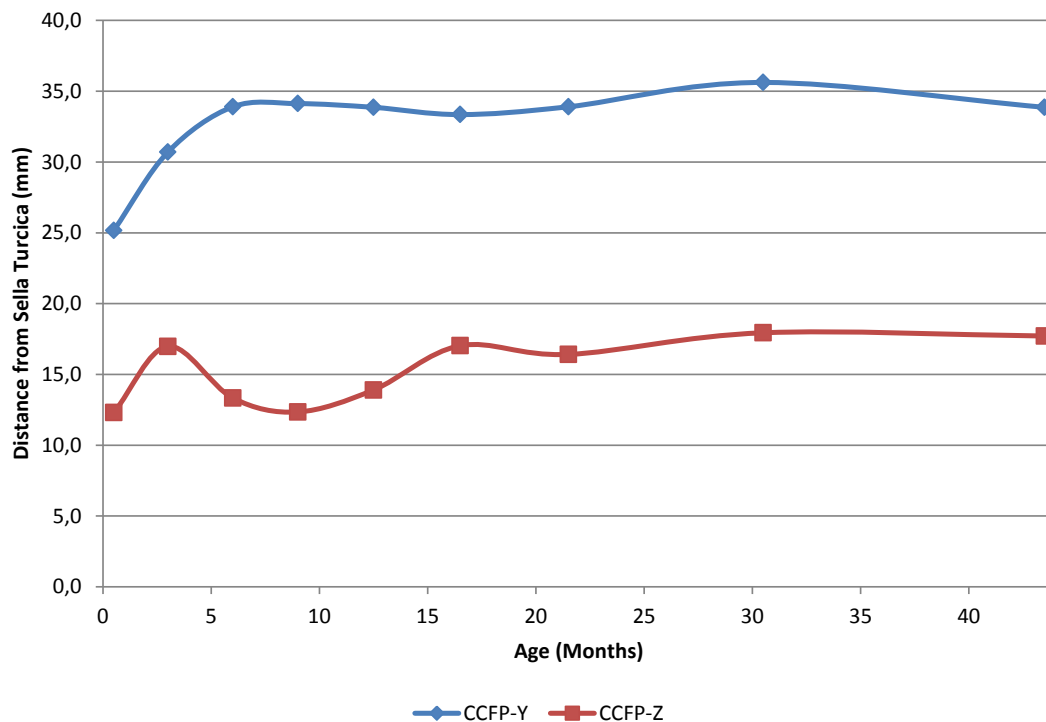


Figure 6.3.1: The mean CCFP Y- and Z- position relative to the sella turcica in the sella turcica-nasion orientation over time.

The results of the mean CCFP Y- and Z- position relative to the sella turcica in the sella turcica-nasion orientation can be seen in [Figure 6.3.1]. The trend for the CCFP-X is ignored since these should float around 0 due to symmetry. Although the CCFP-Z did not show a different mean for the age groups we did perform the trend interpretation for this direction.

The CCFP-Y at the earliest age (0-1 months) starts at 25.2 mm to increase to 30.7 mm at 2-4 months further increasing to 33.9 mm at 5-7 months. There is a minimal decline until 15-18 months to 33.4 mm and a minimal increase until 25-36 months to 35.6 mm. At the latest age of 37-50 months there is a decrease to 33.9 mm. There seems to be an increase in the earlier age to a somewhat stable plateau from 5-7 months old varying between 33.4 mm and 35.6 mm.

The CCFP-Z at the 0-1 months starts at 12.3 mm and increases to 17.0 mm at 2-4 months. There is a decline up to 8-10 months to 12.4 mm followed by an increase to 17.0 mm at 15-18 months. Finally there is a minimum decline to 16.4 mm at 19-24 months old followed by an increase to 17.9 mm old at 25-36 months and 17.7 mm at 37-50 months. There is a rapid increase in the CCFP-Z position after the first measurement moment followed by a decrease that later on follows somewhat of a plateau at 15-18 months and onwards.

6.3.2. Statistical Analysis

The total and mean CCFP values in all directions for the CT-scans were distributed normally as seen by the Shapiro-Wilks Test ($p \geq 0.073$ in all groups). The Levene's Test indicated equal variances for the x-direction [$F = 1.446, p = 0.203$] and z-direction [$F = 1.1914, p = 0.080$] and unequal variances for the y-direction [$F = 3.947, p = 0.001$]. For the x-direction there was no significant difference in means using ANOVA at the $p < 0.05$ level [$F(8,47) = 0.433, p = 0.895$]. For the z-direction there was a significant difference in means using ANOVA at the $p < 0.05$ level [$F(8,47) = 2.354, p = 0.032$]. For the y-direction we performed both a Welch and Brown-Forsythe test. The Welch Test showed a significant differences in means for the z-direction [$F = 6.886, p = 0.001$]. The Brown-Forsythe test showed a significant differences in means for the z-direction [$F = 3.624, p = 0.005$].

Lastly we did a Turkey HSD Post-hoc test to determine which means of the x-direction and z-direction were significantly different from the other groups ($\alpha = 0.05$). None of the means of the age groups were significantly different from other groups for the x-direction and z-direction. We did a Games-Howell Post-hoc test to determine which means in the y-direction were significantly different from the other groups ($\alpha = 0.05$). The only significant difference in means was that of the 0-1 months group with all other groups except for the 2-4 month old group.

6.4. Discussion

The reported mean CCFP end positions for adults using the same CCFP calculation pipeline is (-1.6, 29.9, 18.7) *mm* for the skull [Section 5]. However if we look at the results of the oldest age group of 37–50 months the CCFP end positions are (-0.9, 33.9, 17.7) *mm* for the skull. Considering only the difference in the y- and z-direction we can see that the z-direction is only -1.0 *mm* off from the end position and the y-direction is +4 *mm* off from the mean adult position. We are however missing data on growth between 50 months and 18 years old.

If we regard the population of these healthy children representable we can expect some additional skull morphology and growth between 50 months and 18 years old. Some in depth growth about the human skull is known for this period as shown by *Delye et al. (2015)* and *Waitzman et al. (1992)* [13, 67]. Between 4 and 20 years there is both an increase in the cephalic length, cephalic width and intercoronal distance over time. These values can influence the CCFP position over time and thus can explain the difference between the 4 year old group and adults. Cephalic height or similar as a measure was not given, however this could also influence the CCFP. For future research the evolution of the CCFP for the age 4-20 will be researched.

The overall population size per age group was low. This is due to the limited availability of CT-scans of healthy pediatric patients. We would have preferred if we could distinguish between gender in our analysis as well since there is still debate whether gender has an effect on skull morphology over time [13].

Another issue that there it is uncertain if the CCFP values for the caniosynostosis affected skulls is identical to those of the unaffected ones. It is expected to influence the position of the CCFP however the extend of the influence is not known yet.

6.5. Conclusion

The goal of the study was to describe the morphology of the CCFP in the aging pediatric skull. Although there was a relatively low sample size, a morphology over time became apparent.

Statistical significant difference in the mean CCFP values was only found in the CCFP-Y direction for the 0-1 months group with all other groups except for the 2-4 month old group.

Although the statistical analysis only showed limited significant difference in means, a pattern for the CCFP evolution did emerge. The CCFP-Y value increases over time to stay at a plateau from 5-7 months to 37-50 months. The CCFP-Z value shows a bit more complicated path with first an increase followed by a decrease to later increase again to a plateau that is maintained at 37-50 months old.

The CCFP at the latest age is nearing that of the adult population. The mean CCFP for the 37-50 month group needs to increase 1 mm in the z-direction and decrease 4 mm in the y-direction to achieve the mean

With the determination of the apparent morphology of the CCFP we have found an option to create age specific corrections for e.g. sequential 3D Photos.

References

- [1] Bethany J Slater et al. "Cranial sutures: a brief review." In: *Plastic and reconstructive surgery* 121.4 (2008), 170e–8e. ISSN: 1529-4242. DOI: 10.1097/01.prs.0000304441.99483.97.
- [11] Jeffrey R Marcus et al. "Use of a three-dimensional, normative database of pediatric craniofacial morphology for modern anthropometric analysis." In: *Plastic and reconstructive surgery* 124.6 (2009), pp. 2076–84. ISSN: 1529-4242. DOI: 10.1097/PRS.0b013e3181bf7e1b.
- [13] Hans Delye et al. "Creating a normative database of age-specific 3D geometrical data, bone density, and bone thickness of the developing skull: a pilot study". In: *Journal of Neurosurgery: Pediatrics* 16.6 (2015), pp. 687–702. ISSN: 1933-0707. DOI: 10.3171/2015.4.PEDS1493.

- [14] Jan-Falco Wilbrand et al. "Objectification of cranial vault correction for craniosynostosis by three-dimensional photography." In: *Journal of cranio-maxillo-facial surgery : official publication of the European Association for Cranio-Maxillo-Facial Surgery* 40.8 (2012), pp. 726–30. ISSN: 1878-4119. DOI: 10.1016/j.jcms.2012.01.007.
- [19] Arne Björk. "Cranial base development: a follow-up x-ray study of the individual variation in growth occurring between the ages of 12 and 20 years and its relation to brain case". In: *American Journal of Orthodontics* (1955). DOI: 10.1016/0002-9416(55)90005-1.
- [27] G. A. De Jong, T. J J Maal, and H. Delye. "The computed cranial focal point". In: *Journal of Cranio-Maxillofacial Surgery* 43.9 (2015), pp. 1737–1742. ISSN: 18784119. DOI: 10.1016/j.jcms.2015.08.023.
- [67] A. A. Waitzman et al. *Craniofacial skeletal measurements based on computed tomography: Part II. Normal values and growth trends*. 1992. DOI: 10.1597/1545-1569(1992)029<0118:CSMBOC>2.3.CO;2.

7 | Radiation-free 3D head shape and volume evaluation after endoscopically assisted strip craniectomy followed by helmet therapy for trigonocephaly

Parts of this chapter were presented or are to be presented at the following events:

- Oral presentation at ESPN 2016, Paris, 25th Congress of the European Society for Pediatric Neurosurgery, 8-11 May 2016
- Oral presentation at ISPN 2016, Kobe (Japan), 44th Annual Meeting of the International Society for Pediatric Neurosurgery, 23-27 October 2016

This chapter was submitted to Journal of Cranio-Maxillo-Facial Surgery at 15th of August 2016 for review.

7.1. Introduction

Craniosynostosis is the premature fusion of cranial sutures occurring at 1 in 2000 to 1 in 2500 live births [1]. Treatment for cranyiosynostosis comes with different approaches. Trigonocephaly has two main approaches; the open cranial vault reconstruction and (endoscopic) suturectomy with spring- or /helmet therapy [4, 5, 6, 7, 9, 8]. Objective comparison, follow-up and evaluation of these approaches remain difficult. Modern clinical diagnosis of head shapes and follow-up after surgical craniosynostosis interventions usually relies on the use of CT-scans, cranial x-rays and in the past few years also three dimensional (3D) photogrammetry [10, 11, 12, 13, 68, 15, 14]. 3D Photogrammetry using 3D Photo systems were introduced as a radiation-free alternative but are limited to capturing soft tissue surfaces lacking the bony structures used in traditional follow-up. However it is possible to use 3D photos for objective follow-up. A common reference

point for skull comparison is the sella turcica since its relative position is assumed to be more or less stable during skull growth [19]. A new method to determine a similar reference point, the computed cranial focal point (CCFP), was proposed using a 3D surface from a 3D Photo [27]. The CCFP has a fixed location relative to the sella turcica. This allows orienting 3D photos of the head in the sella turcica-nasion plane anchored to the sella turcica for radiation-free longitudinal follow-up.

Since it is possible to perform radiation-free longitudinal follow-up using 3D photos and we want to initiate this practice by describing our methodology for this follow-up as well as the results for the endoscopically assisted craniosynostosis surgery. At our institute we have database of 3D photos of patients that underwent this surgery. Using the CCFP for registration of 3D photos we are able to perform longitudinal evaluations.

The goal of this chapter is to evaluate the head shape changes over time to determine the shape and volume growth pattern in patients that underwent endoscopically assisted craniosynostosis surgery. We look at the longitudinal volume change of the anterior fossa and the total head. The anterior fossa volume is of interest due to being the volume in the affected region of the head. We compare these volumes changes in CT-scans with a reference group of children that did not undergo this surgery.

7.2. Materials and Methods

Since December 2010 we used 3D photography in our craniosynostosis follow-up using a 3DMDhead System (3dMD Limited, Londen United Kingdom) in RadboudUMC, Nijmegen, the Netherlands. In our follow-up database we selected all 3D photos of children that underwent endoscopically assisted metopic craniosynostosis surgery with helmet therapy that had a pre-surgery 3D photo and at least one post-surgery 3D photo. 26 Patients were identified that met these criteria of which we evaluated the head shape and volume changes over time up to October 2015. The 3D photos were grouped according to age between 2 and 48 months old [Table 7.2.1].

Table 7.2.1: Number of patients included in each age group for 3D Photos and CT-scans. * = Pre-surgery patients.

| Group | Age (months) | 3D Photos | CT-scans |
|-------|--------------|-----------|----------|
| 1 | 2-4 | 22* | 6 |
| 2 | 5-7 | 4* | 3 |
| 3 | 8-10 | 17 | 4 |
| 4 | 11-14 | 14 | 11 |
| 5 | 15-18 | 8 | 8 |
| 6 | 19-24 | 8 | 8 |
| 7 | 25-36 | 8 | 5 |
| 8 | 37-48 | 5 | 8 |

Each 3D photo underwent orientation in a reference frame and resampling. Volumes of anterior fossa and whole head were determined and analyzed. The volumes of the heads of the 3D photos were compared to volumes of healthy children, based on CT-scan calculations. We defined healthy if the CT-scan showed no pathological, traumatic, or morphological changes of the bony tissue of the head as well as the absence of hydrocephalus or tumors. The CT-scans were acquired of children that underwent a head CT-scan at the emergency room and were between 2 and 48 months old. CT-scans were used as a reference since we do not have a 3D photo set of healthy children yet. Average head shapes and normalized average head shapes per group were made for shape evaluation over time.

7.2.1. Orientation and Resampling

We compared the volume pattern differences between the CT-scans and 3D photos as well as the morphology of the head based on the 3D photos. In order to perform these measurements we had to orient the CT-scans and 3D photos in the same reference frame. These steps are displayed in the flowchart in [Figure 1]. Orientating the 3D photos in the reference frame of the CT-scan was executed by determining an age-specific CCFP to sella turcica offset using the CT-scans. This offset is used to approximate the sella turcica in the 3D photos prior to positioning these in the sella turcica nasion reference frame. The offset is already calculated in [Section sec:child]. Once the CT-scans and 3D photos were registered in the reference frames the age specific volumes could be determined as well as the mean shapes for the 3D photos. In depth information on these steps can be found in the appendix [Section 7.6.1]. All calculations were performed using Matlab 2015a (8.5) [28] with C++ and OpenCL 1.2 [22].

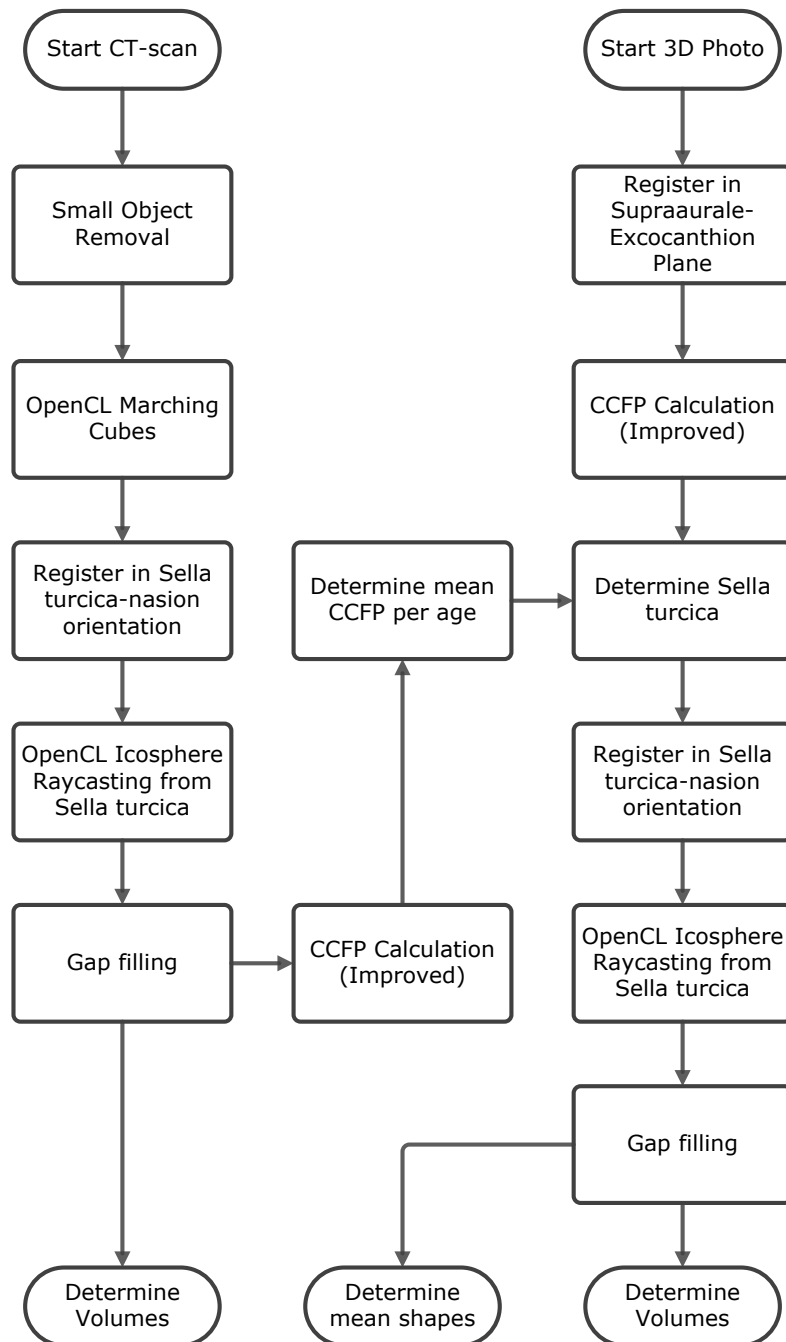


Figure 7.2.1: Flowchart to determine the mean shape per age group for 3D photos and the mean volume per age group for CT-scans and 3D photos.

7.2.2. Volume Analysis

For both the CT-scans and 3D Photos in each age group the mean volume, standard deviation and range of volumes were calculated above the sella turcica-nasion plane as well as for the anterior part of the head. We defined the anterior part of the head by the volume above the sella turcica-nasion plane and the volume in front of the plane crossing the center of the sella turcica perpendicular to both the sella turcica-nasion plane and the mid-sagittal plane. This approximates the anterior cranial fossa. Additionally the ratio between the anterior part and the entire head was calculated. The outer skin layer of the skull in the CT-scans was incomplete in the majority of the cases hence we used the outer bony surface for the CT-scan volume calculations.

Since we used two different surfaces on which we determine the volumes (skin for 3D and skull for CT), we only compared the patterns of the volumes and volume ratios between the surgery group and reference group.

7.2.2.1. Statistical Analysis

We compared the means of the volumes of the patients per age group for the total volume and anterior volume to determine if there was a significant difference. We started with a Shapiro-Wilks Test to test for normality. We also performed a Levene's Test to test the Homogeneity of Variances. We further executed a Brown Forsythe and Welch Test instead of the ANOVA test since the homogeneity of variances was not met. Lastly we used a Games-Howell Post-hoc test to determine which means were significantly different from the other groups ($\alpha = 0.05$).

7.2.3. Shape Analysis

Shape analysis between age groups was performed by comparing the average head shape per age group. Heatmaps were generated to show the absolute and normalized change between two sequential age groups. We were able to interpolate between two age groups for the vertex position and heatmap color. We used interpolation on the heatmaps to create animations of the average absolute shape change with the corresponding heatmap [Digital thesis only].

For the shape analysis we grouped the 3D Photos to their respective follow-up time since we were interested in the effect of the surgery. The group distribution for the shape analysis can be seen in [Table 7.2.2].

Table 7.2.2: *Number 3D Photos of trigonocephaly patients per group.*

| Group | # 3D Photos |
|---------------------------|-------------|
| Pre-surgery | 26 |
| 6 Months post-surgery | 21 |
| 12 Months post-surgery | 19 |
| 18 Months post-surgery | 8 |
| 24 Months post-surgery | 8 |
| 36-48 Months post-surgery | 4 |

7.3. Results

7.3.1. Volume Analysis

The mean total and mean anterior head volumes above the sella turcica-nasion plane of the 3D photos can be seen in [Table 7.3.1] and [Figure 7.3.1]. The mean total volume starts at 942 ml and increases to 1846 ml (96.0% incline). The mean anterior volume starts at 308 ml and increases to 664 ml (116.0% incline). The volumes are based on the outer skin layer as observed by the 3D camera.

Table 7.3.1: *Outer skin trigonocephaly 3D photo head volume measurement above the sella turcica-nasion plane per group. * = Pre-surgery patients.*

| Group | n | Total Volume (ml) | | | Anterior Volume (ml) | | | Ratio |
|------------------|----|-------------------|-------------|-----|----------------------|-----------|-----|---------|
| | | Mean | Range | Std | Mean | Range | Std | A/T (%) |
| 1 (2-4 months)* | 22 | 942 | [748–1110] | 98 | 308 | [233–380] | 38 | 32.7 |
| 2 (5-7 months)* | 4 | 1205 | [1011–1378] | 184 | 489 | [311–586] | 86 | 37.2 |
| 3 (8-10 months) | 17 | 1287 | [1055–1614] | 131 | 491 | [464–518] | 52 | 38.1 |
| 4 (11-14 months) | 14 | 1400 | [1133–1670] | 172 | 524 | [480–567] | 74 | 37.4 |
| 5 (15-18 months) | 8 | 1463 | [1318–1697] | 133 | 528 | [478–679] | 60 | 36.1 |
| 6 (19-24 months) | 8 | 1467 | [1281–1627] | 106 | 521 | [485–579] | 44 | 35.5 |
| 7 (25-36 months) | 8 | 1616 | [1361–1901] | 165 | 568 | [501–634] | 79 | 35.1 |
| 8 (37-48 months) | 5 | 1846 | [1717–2007] | 110 | 664 | [590–739] | 60 | 36.0 |

The mean total and mean anterior head volumes above the sella turcica-nasion plane of the CT-scans can be seen in [Table 7.3.2] and [Figure 7.3.1]. The mean total volume starts at 818 ml and increases to 1396 ml (73.5% incline). The mean anterior volume starts at 262 ml and increases to 454 ml (70.8% incline). The volumes are based on the outer bony skull layer of the CT-scan.

Table 7.3.2: Outer skull reference CT head volume measurement above the sella turcica-nasion plane per group.

| Group | n | Total Volume (ml) | | | Anterior Volume (ml) | | | Ratio |
|------------------|----|-------------------|-------------|-----|----------------------|-----------|-----|---------|
| | | Mean | Range | Std | Mean | Range | Std | A/T (%) |
| 1 (2-4 months) | 6 | 818 | [687–1153] | 174 | 262 | [213–378] | 69 | 32.0 |
| 2 (5-7 months) | 3 | 1067 | [1047–1105] | 33 | 371 | [367–374] | 4 | 34.7 |
| 3 (8-10 months) | 4 | 1143 | [1081–1239] | 68 | 412 | [378–445] | 30 | 33.1 |
| 4 (11-14 months) | 11 | 1196 | [995–1390] | 116 | 423 | [337–515] | 63 | 35.3 |
| 5 (15-18 months) | 8 | 1249 | [1119–1400] | 90 | 412 | [348–508] | 51 | 33.0 |
| 6 (19-24 months) | 8 | 1324 | [1208–1505] | 91 | 440 | [385–518] | 40 | 33.3 |
| 7 (25-36 months) | 5 | 1413 | [1263–1577] | 119 | 460 | [394–509] | 42 | 32.5 |
| 8 (37-48 months) | 8 | 1396 | [1269–1624] | 113 | 454 | [398–606] | 67 | 32.5 |

Since we used two different surfaces (skin for 3D and skull for CT), we only compared the patterns of the volumes and anterior/total-ratios between the surgery group and reference group. Looking at the volumes over time [Figure 7.3.1] we can see that both the surgery group and reference group follow a similar growth pattern with some minor differences. One difference is that the surgery group still shows an increase in growth both total and anteriorly volume after 36 months (group 8) of age while the reference group does not. Another observation is that there is a plateau between 15 and 24 months old (group 5 & 6) for the mean total volume and mean anterior volume growth in the surgery group. A similar plateau can be observed between 8 and 18 months old (groups 3-18) for the mean anterior volume growth of the reference group.

The anterior/total-ratio of both groups is shown in [Figure 7.3.2]. Again we see a similar ratio pattern. Both groups start at a lower ratio to increase in ratio until the age of 8-10 month. From here on there is a decline up to the 25-36 month group. A small incline could be observed in between for the reference group at 19-24 months old. The ratio stays near equal for the reference group until 37-48 months of age while the trigonocephaly group still shows a slight increase from 35.1 to 36 %.

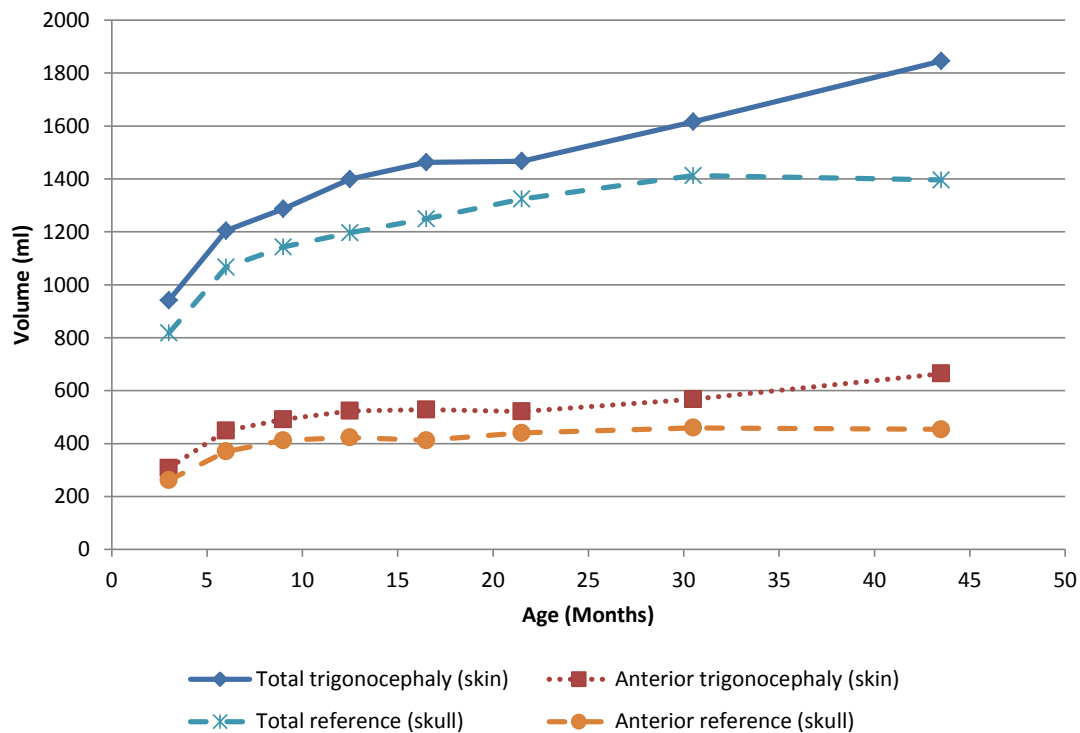


Figure 7.3.1: Average volumes of the full and anterior part of the head above the sella turcica-nasion plane for the trigonocephaly group (skin) and reference group (skull).

7.3.1.1. Comparison of anterior growth percentages

Table 7.3.3: Anterior growth progress and relative growth for the trigonocephaly and reference groups. The growth process shows the percentage of growth achieved. The relative growth shows the percentage of difference in volume compared to the previous group.

| Group | Growth Progress (%) | | Relative Growth (%) | |
|------------------|---------------------|-----------|---------------------|-----------|
| | Trigonocephaly | Reference | Trigonocephaly | Reference |
| 2 (5-7 months) | 39.5 | 56.8 | 45.8 | 41.7 |
| 3 (8-10 months) | 51.4 | 78.4 | 9.5 | 11.2 |
| 4 (11-14 months) | 60.5 | 83.8 | 6.6 | 2.5 |
| 5 (15-18 months) | 61.9 | 78.5 | 0.9 | -2.5 |
| 6 (19-24 months) | 59.9 | 93.1 | -1.3 | 6.8 |
| 7 (25-36 months) | 72.8 | 103.1 | 8.8 | 4.4 |
| 8 (37-48 months) | 100.0 | 100.0 | 17.1 | -1.3 |

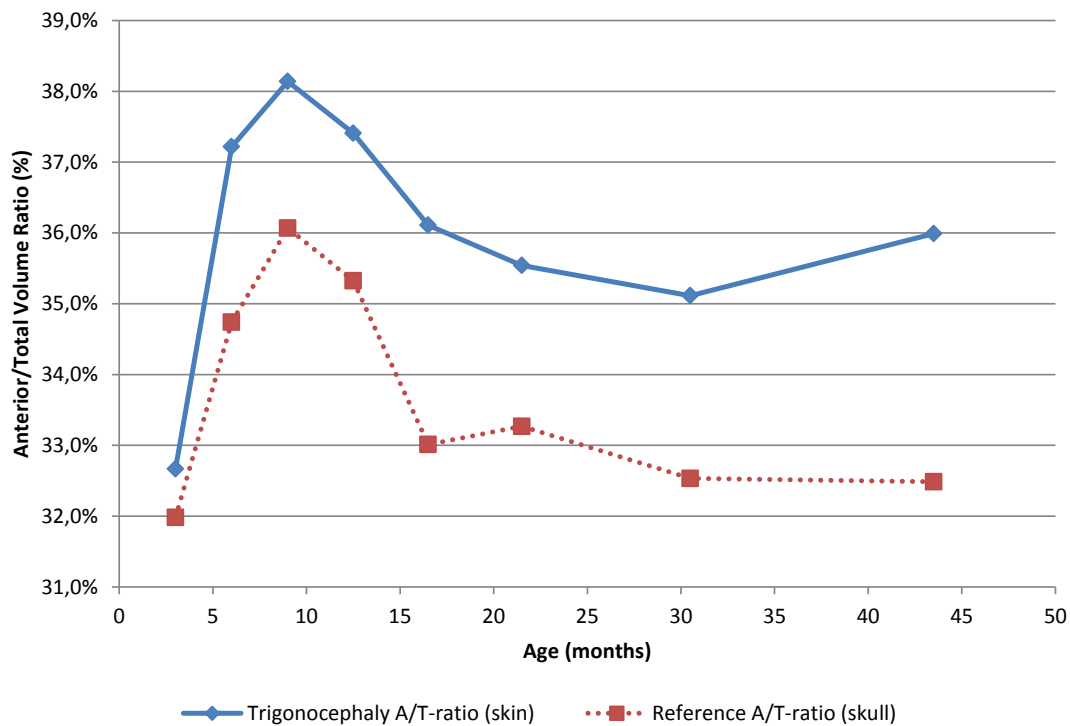


Figure 7.3.2: Average volume ratio between the full and anterior part of the head above the sella turcica-nasion plane for the trigonocephaly group (skin) and reference group (skull).

The results of the anterior growth comparison between the surgery group and reference group can be seen in [Table 7.3.3]. We distinguish between two measures: the growth progress (percentage of total volume achieved starting at group 1 with 0%) and the relative growth (percentage of difference in volume compared to the previous group). The surgery group starts with 39.5% of the growth progress completed at 5-7 months old whereas the reference group already completed 56.8%. The reference group progress goes up to 78.4% at 8-10 months old while the surgery group only achieves 51.4%. A small plateau is present for the reference group up till 15-18 months old at around 80%. The surgery group growth progress will go to 60.5% at 11-14 months to stay at a plateau up to 19-24 months old (59.9%). The reference group achieved full growth for our observation window at 25-36 months old. The surgery group has a steady increase from 19-24 months old to 37-48 months old achieving full growth for our observation windows without the plateau as observed at the reference group.

7.3.1.2. Statistical Analysis

The total and anterior volumes for the 3D Photos were distributed normally as seen by the Shapiro-Wilks Test ($p \geq 0.255$ in all groups). The Levene's Test indicated equal variances for the total volumes ($F = 1.556$, $p = 0.161$) and unequal variances for the anterior volumes

($F = 2.273, p = 0.037$). However, the ratio between the minimum and maximum variances are 3.5 for the total volumes and 4.9 for the anterior volumes. Thus equal variances can not be assumed. The Welch Test showed a significant differences in means for both the total volumes ($F = 56.164, p < 0.001$) and anterior volumes ($F = 40.758, p < 0.001$). The Brown-Forsythe shows a similar result for the total volumes ($F = 50.203, p < 0.001$) and anterior volumes ($F = 32.225, p < 0.001$).

Lastly we did a Games-Howell Post-hoc test to determine which means were significantly different from the other groups ($\alpha = 0.05$). The total volume means of the 2-4 month group was significantly different from all other groups except for the 5-7 month group. The 37-48 month group was significantly different for the mean total volumes from all groups except the 25-36 month group. The 8-10 month group was significantly different from the 19-24 month, 25-36 month, and 37-48 month group for the mean total volumes.

For the mean anterior volumes the 2-4 month group was significantly different from all other groups except for the 5-7 month group. The 37-48 month group was significantly different for the mean total volumes from all groups except the 25-36 month and 5-7 month group.

7.3.2. Shape Analysis

7.3.2.1. Absolute Shape

The average growth and shape change over time in *mm* can be seen in [Figure 7.3.3]. In the first 6 months post surgery there is a predominant growth around the frontal and occipital area of the head up to 8 mm along with growth of the orbital rims. The strip site shows the least growth in the frontal region [Figure 7.3.3 Top-left]. Between the period of 6 to 12 months post surgery you can see the most growth on and around the site where the strip was removed peaking up to 5 mm along with more frontal growth of the orbital rim area [Figure 7.3.3 Top-right]. Between 12 and 18 months old there is an overall growth in the frontal area peaking 3 mm [Figure 7.3.3 Middle-left]. No notable growth above 1 mm can be found between 18 to 24 months old except for growth of the orbital rims and the occipital area [Figure 7.3.3 Middle-right]. Between 24 and 36-48 months old the growth is focused at the temporal area of the head [Figure 7.3.3 Bottom-left].

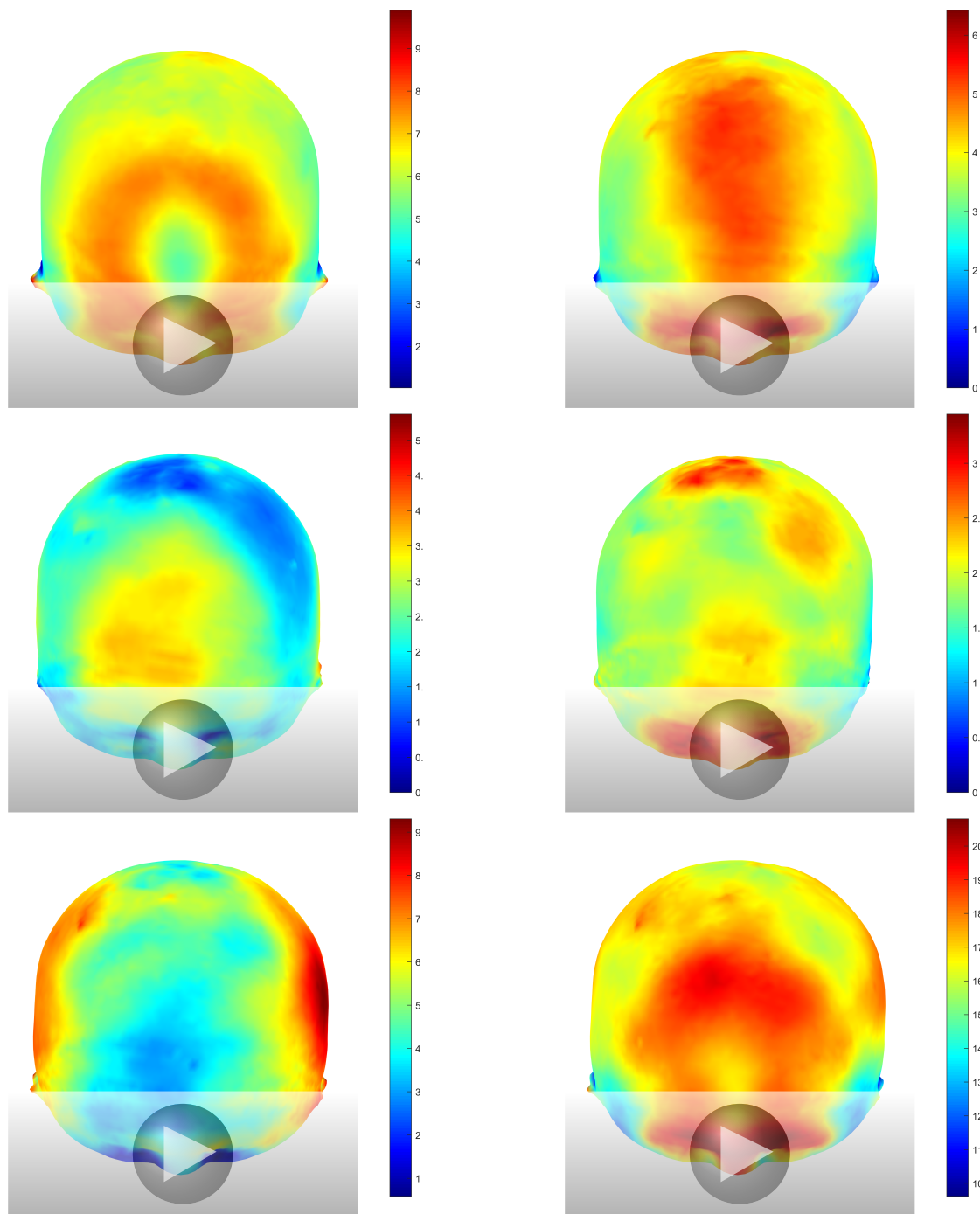


Figure 7.3.3: Mean head shapes with heatmaps of the absolute head growth in mm for the trigonocephaly group (Please note the different color scales). Top-left: Pre-surgery to 6 months post-surgery. Top-right: 6 to 12 months post-surgery. Middle-left: 12 to 18 months post-surgery. Middle-right: 18 to 24 months post-surgery. Bottom-left: 24 months post-surgery to 36-48 months post-surgery. Bottom-right: pre-surgery to 36-48 months post-surgery.

The total growth from Pre-surgery to 36-48 months post surgery indicates the strongest

growth along the orbital rims and below the anterior fontanel [Figure 7.3.3 Bottom-right]. Furthermore a considerable amount of growth can be found near the centers of the parietal bones. The sphenoid wing, and temporal bone show the smallest amount of growth. No predominant orbital widening seems to occur over time.

7.3.2.2. Normalized Shape

The normalized growth and shape changes per time in percentage can be seen in [Figure 7.3.4]. Normalized growth ensures that the volume over time stays equal, showing relative growth. This means that if there is relative growth at one site, relative shrinkage must occur at the rest of the head. Between pre-surgery and 5 months post surgery we see a relative growth around the surgery site, orbital rims, temporal bone and occipital area [Figure 7.3.4 Top-left]. In the center of the frontal bone is an area with relative shrinkage. Between 6 months and 12 months there is a similar growth to the absolute shape change [Figure 7.3.4 Top-right]. Between 12 to 18 months old there is relative growth in the overall frontal area and the left occipital area [Figure 7.3.4 Middle-left]. The latter is most likely an artifact due to naturally occurring asymmetry and sample size. Between 18 and 24 months old there is a relative growth of the orbital rims and the occipital area [Figure 7.3.4 Middle-right]. In the group from 24 to 36-48 months old there is a predominant growth in the temporal area of the head [Figure 7.3.4 Bottom-left].

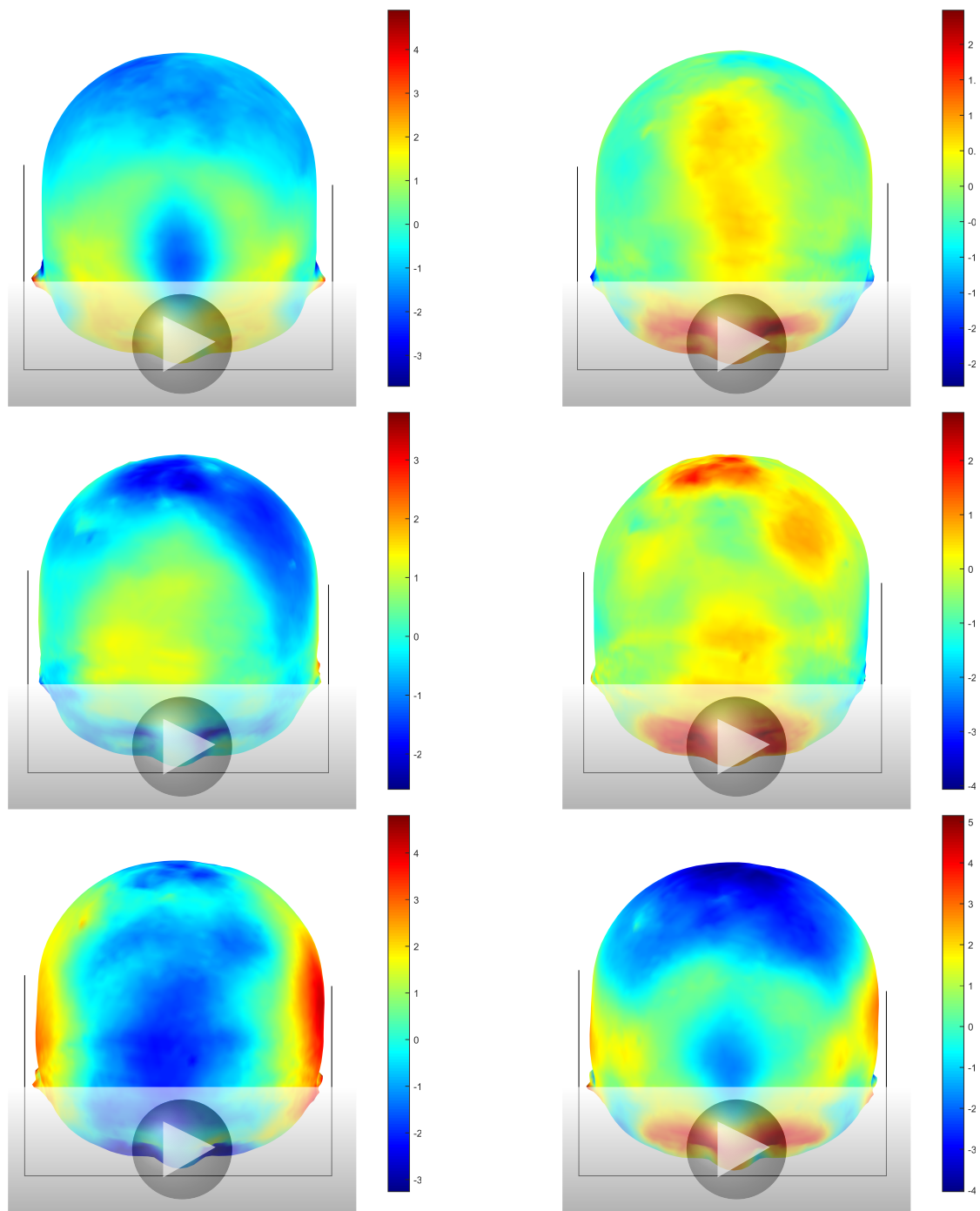


Figure 7.3.4: 3D* Normalized mean head shapes with heatmaps of the normalized head growth in mm for the trigonocephaly group (Please note the different color scales). Top-left: Pre-surgery to 6 months post-surgery. Top-right: 6 to 12 months post-surgery. Middle-left: 12 to 18 months post-surgery. Middle-right: 18 to 24 months post-surgery. Bottom-left: 24 months post-surgery to 36-48 months post-surgery. Bottom-right: pre-surgery to 36-48 months post-surgery.

When looking from pre-surgery to 36-48 months post surgery we see a growth in the

orbital rims, below the frontal fontanel and the temporal to occipital area of the head [Figure 7.3.4 Bottom-right]. In the frontal center of the frontal bone there is a relative shrinkage equal to that of the cranial part of the parietal bones.

7.4. Discussion

With the use of the CCFP and 3D Photos it is possible to perform a longitudinal radiation free follow-up of head shape and volume. The current population on which this was performed consisted of patients that underwent endoscopically assisted metopic suture craniosynostosis surgery. We have started in December 2010 to create full head 3D Photos of children with craniosynostosis pre- and post-surgery over time. So far only 27 patients could be used in the follow-up with in total 86 usable 3D Photos on which we based our analysis. This analysis already shows the initial results whereas we keep expanding our database with more 3D Photos to further improve this analysis.

We compared the growth patterns between patients that underwent endoscopically assisted metopic suture craniosynostosis surgery and a reference group of healthy children using two different modalities. The different modalities were chosen based on the availability in our clinic. Because of the difference between these two modalities we also have a difference in the segmented/observed surface and thus volume. The bony outer surface will always result in a smaller volume compared to the skin outer surface. Unfortunately, CT-scans of healthy children that include the complete skin surface are very scarce and we had to use the outer bony surface in order to obtain enough CT-scan data for the reference group. However, this limited our study by only comparing the growth patterns between our reference group and surgery group and not the absolute volumes. Using a correction value as determined by McKay et al. for volumes above the lateral canthus and tragus could be an option to correct for the sella turcica-nasion plane if determined [15]. In our case these correction values of the total mean ct-scan outer bony surface volumes to the total mean trignoncephaly skin surface volume values would be between 1.11 and 1.17 depending on the age (nonlinear). However since these correction values are between the skull of normal reference groups and the skin of surgery groups we did not use these correction values.

For the growth and shape analysis we used different grouping as compared to the volume analysis. This was done to monitor the growth and shape effects caused by the surgery in detail. However we did not have reference 3D photos of healthy children. If we do, we can distinguish shape changes caused by natural growth and those that are caused by the surgery. We are currently building a database with 3D Photos of healthy children for future research.

The absolute and relative shape analysis showed growth around the surgical site with a

relative shrinkage at the center of the frontal bone. Skull widening occurs in the later phase after surgery. Although there is a considerable amount of growth at the orbital rims, we did not see orbital widening in this time frame. Absolute growth at the sphenoid wing and temporal bone show an overall smallest growth of the entire analyzed area.

Other studies that evaluated shape changes either in pre- to post-surgery or long-term are often limited to a selection of parameters and not the whole head growth analysis [68, 10]. Analysis of using the whole head shape in sagittal craniosynostosis have been done before, however still using CT-scans [11]. Longitudinal whole head shape analysis of metopic suture craniosynostosis was not performed in earlier research to our best knowledge.

The mean anterior volume, mean total volume and A/T-ratio showed a near similar pattern over time. Although some differences were observed. When looking at the volume pattern it can be seen that there is a small plateau in the surgery group for both the mean total and mean anterior volume at 15 to 24 months. This could potentially point towards slowing down of the growth although this could also be due to our limited sample size. The mayor difference can be observed at 37-48 months old. The patient group still shows some additional volume growth (+ 0.9%) while the reference group does not. Statistically there was no difference between the means of the volumes at 24-36 months and 37-48 months. So it could be that this effect is caused by our sample size.

Intracranial volume measurement in craniosynostosis has been done before [69, 70, 71, 72]. However these are limited to pre-surgery [69, 70, 71], or only compare pre- to post-surgery [72]. The pre- to post-surgery comparison did include the anterior fossa to total volume analysis, but was limited to brachycephalic craniosynostosis. One of the latest study involving total volume analysis was done for sagittal synostosis [73]. Since sagittal synostosis affects a larger area of the skull there is no need for partial volume analysis like in trigonocephaly. To our knowledge no longitudinal follow-up of the volumes in after metopic suture craniosynostosis surgery exist to date.

Using an objective measure significantly helps in the evaluation and quantification of the effects of craniosynostosis interventions. This is not only the case for our institution, but also for others around the world performing craniosynostosis interventions. The current 3D camera systems are getting cheaper and more accessible for both the mainstream and professional clients. Using these 3D cameras and new analysis techniques as shown in this study can help with reducing the amount of preventable ionizing radiation that is used in craniosynostosis follow-up. We hope that by the method shown in this study more institutes performing craniosynostosis surgery will use 3D photos or retrospective CT-scans to further quantify the effects of the surgery. We further hope to provide a method to objectively compare and further improve craniosynostosis surgery.

7.5. Conclusion

We performed a retrospective study to evaluate the head shape and volume changes over time after endoscopically assisted metopic craniosynostosis surgery. We have been able to analyze the volume changes over time above the sella nasion plane thanks to the use of the CCFP [27]. The mean total and anterior head volume growth pattern was almost equal to the reference group. A total mean volume increase of 96.0% and an anterior mean increase of 116.0% was observed in the surgery group.

The A/T-ratio pattern is also nearly similar in both groups. Again a deviation occurs at the later age from the 24-36 months to 37-48 months. The A/T-ratio for the surgery group increases while the reference group stays equal.

When looking at the overall growth progress of the mean anterior volume of both groups, we observed that the reference group was at the final anterior volume earlier than the surgery group and had a stronger incline at the start.

The shape analysis showed the growth pattern over time both absolute and relative. The surgical site and orbital rims show the most prominent growth along with the center of the parietal bones. The site of the removed strip showed the least local growth of the anterior portion of the head. The shape analysis shows the smallest growth in the orbital widening, sphenoid wing, and temporal bone over the evaluated period.

Our method for head shape and volume analysis gives insight in the growth pattern after endoscopically assisted metopic craniosynostosis intervention. This method can be used for healthy patients as well as other forms of craniosynostosis evaluation in the future. We hope that other institutes adapt and possibly improve this methodology to objectively compare the longitudinal effects of craniosynostosis surgery as well to further improve this surgery.

7.6. Appendix

7.6.1. Orientation Procedure

7.6.1.1. CT-scans

For the orientation of the CT-scans we start by removing small objects in the scan with a 167 HU intensity or above. We created the surface data by using an OpenCL accelerated marching cubes algorithm also at 167 HU [50]. The CT-scans were manually placed in the sella turcica-nasion orientation.

After orientation resampling was performed using raycasting for the sampling [21] on

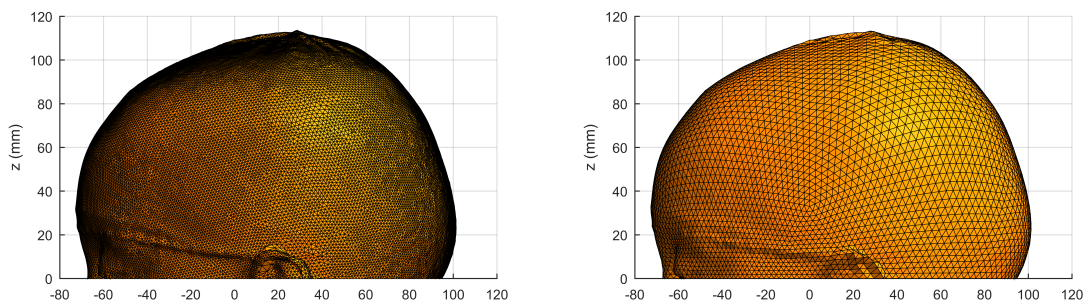


Figure 7.6.1: 3D Photo before (left) and after (right) resampling after orientation. The original version has 106268 triangles and the resampled version has 10240 triangles.

the vertices (3D points) of a hemi-icosphere as reference shape. Resampling reduces the amount of 3D points used to describe an object while maintaining the overall shape [Figure 7.6.1]. Using a reference shape enables simple mathematical and statistical analysis. The number of vertices was chosen as low as possible for less computation time while ensuring that the inaccuracy of the CCFP [27] position caused by sampling would be less than 1 *mm*.

Gaps in the resampled surface can occur naturally or by the CT-scan scanning procedure. The gaps were filled by iteratively determining the 3D points based on the average position of the neighborhood of neighboring 3D points to the origin.

After filling the gaps the CCFP position and volumes were determined and averaged per age. The CCFP is later used to determine the sella turcica position in the 3D photos of the same age group. An improved CCFP calculation was used that weights triangle size differences that can occur in 3D Photos [Section 5.6.1].

7.6.1.2. 3D Photos

The 3D photos were manually placed in a supraaurale-exocanthion orientation. The origin was placed at the midsagittal plane crossing the line between the two exocanthions. We determined the CCFP position using the surface that was at 20 mm above the supraaurale-exocanthion plane after a 20 degree anterior rotation [Figure 7.6.2].

We use the CCFP-sella turcica offset from the CT-scans of the same age group and the CCFP position in the 3D photo to calculate the center of the sella turcica in the 3D photo. We translate the 3D photo so that (0,0,0) position is the center of the calculated sella turcica. We rotate the 3D photo so that the head was positioned in the sella turcica-nasion plane.

Gap filling was performed similarly as in the surface of the CT-scans. Finally the mean volumes and the mean shapes per age group were determined for the 3D photos. The mean shapes consisted of the absolute shape as well as the normalized shape. The normalized shape is the absolute shape scaled by the inverse of the cubic root of the volume. These normalized

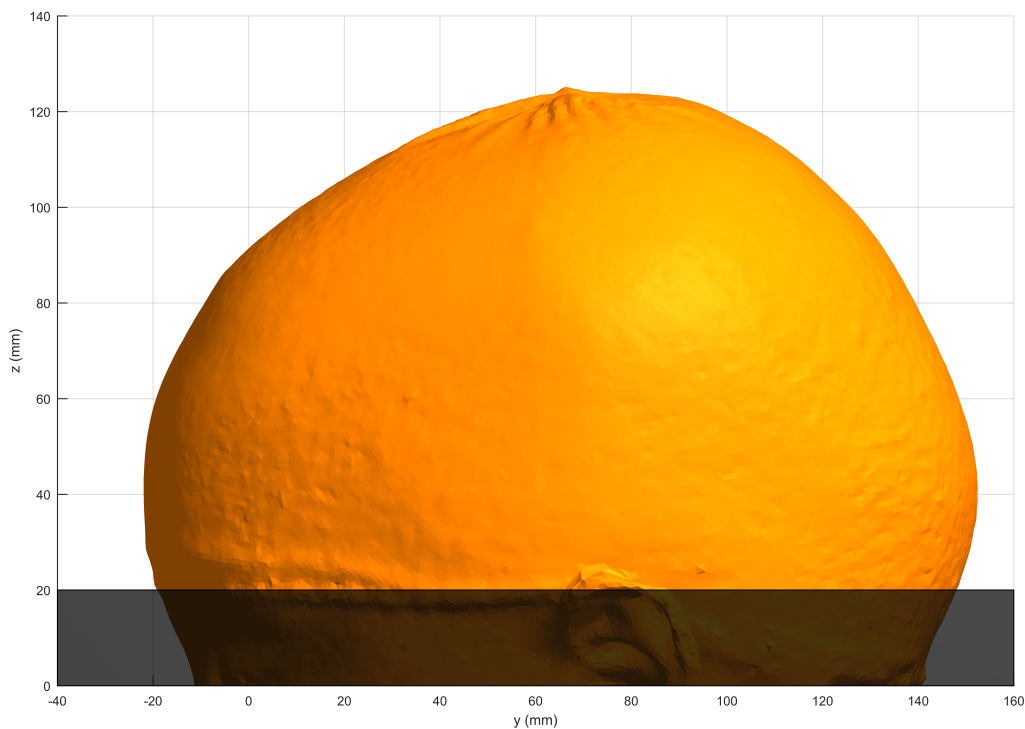


Figure 7.6.2: 3D Photo after pre-orientation. The highlighted area is used CCFP calculation.

shapes have an equal volume regardless of the age group and thus only shape is different.

References

- [1] Bethany J Slater et al. "Cranial sutures: a brief review." In: *Plastic and reconstructive surgery* 121.4 (2008), 170e–8e. ISSN: 1529-4242. DOI: 10.1097/01.prs.0000304441.99483.97.
- [4] Sassan Keshavarzi et al. "Variations of Endoscopic and Open Repair of Metopic Craniosynostosis". In: *Journal of Craniofacial Surgery* 20.5 (2009), pp. 1439–1444. ISSN: 1049-2275. DOI: 10.1097/SCS.0b013e3181af1555.
- [5] J. Hinojosa. "Endoscopic-assisted treatment of trigonocephaly". In: *Child's Nervous System* 28.9 (2012), pp. 1381–1387. ISSN: 02567040. DOI: 10.1007/s00381-012-1796-7.
- [6] Fatma Ozlen et al. "Surgical treatment of trigonocephaly: technique and long-term results in 48 cases." In: *Journal of neurosurgery. Pediatrics* 7.3 (2011), pp. 300–10. ISSN: 1933-0715. DOI: 10.3171/2010.12.PEDS10359.
- [7] D F Jimenez and C M Barone. *Endoscopic craniectomy for early surgical correction of sagittal craniosynostosis*. 1998. DOI: 10.3171/jns.1998.88.1.0077. URL: <http://www.ncbi.nlm.nih.gov/pubmed/9420076>.

- [8] David F Jimenez et al. "Early management of craniosynostosis using endoscopic-assisted strip craniectomies and cranial orthotic molding therapy." In: *Pediatrics* 110.1 Pt 1 (2002), pp. 97–104. ISSN: 0031-4005. DOI: 10.1542/peds.110.1.97.
- [9] C M Barone and D F Jimenez. "Endoscopic craniectomy for early correction of craniosynostosis." In: *Plastic and reconstructive surgery* 104.7 (1999), 1965–73; discussion 1974–5. ISSN: 0032-1052. DOI: 10.3171/jns.1998.88.1.0077.
- [10] JR Marcus, LF Domeshek, and Rajesh Das. "Objective three-dimensional analysis of cranial morphology." In: *Eplasty* 8 (2007), pp. 175–187.
- [11] Jeffrey R Marcus et al. "Use of a three-dimensional, normative database of pediatric craniofacial morphology for modern anthropometric analysis." In: *Plastic and reconstructive surgery* 124.6 (2009), pp. 2076–84. ISSN: 1529-4242. DOI: 10.1097/PRS.0b013e3181bf7e1b.
- [12] Nikoo R Saber et al. "Generation of normative pediatric skull models for use in cranial vault remodeling procedures." In: *Child's nervous system : ChNS : official journal of the International Society for Pediatric Neurosurgery* 28.3 (2012), pp. 405–10. ISSN: 1433-0350. DOI: 10.1007/s00381-011-1630-7.
- [13] Hans Delye et al. "Creating a normative database of age-specific 3D geometrical data, bone density, and bone thickness of the developing skull: a pilot study". In: *Journal of Neurosurgery: Pediatrics* 16.6 (2015), pp. 687–702. ISSN: 1933-0707. DOI: 10.3171/2015.4.PEDS1493.
- [14] Jan-Falco Wilbrand et al. "Objectification of cranial vault correction for craniosynostosis by three-dimensional photography." In: *Journal of cranio-maxillo-facial surgery : official publication of the European Association for Cranio-Maxillo-Facial Surgery* 40.8 (2012), pp. 726–30. ISSN: 1878-4119. DOI: 10.1016/j.jcms.2012.01.007.
- [15] Douglas R McKay et al. "Measuring cranial vault volume with three-dimensional photography: a method of measurement comparable to the gold standard." In: *The Journal of craniofacial surgery* 21.5 (2010), pp. 1419–22. ISSN: 1536-3732. DOI: 10.1097/SCS.0b013e3181e3181e92a.
- [19] Arne Björk. "Cranial base development: a follow-up x-ray study of the individual variation in growth occurring between the ages of 12 and 20 years and its relation to brain case". In: *American Journal of Orthodontics* (1955). DOI: 10.1016/0002-9416(55)90005-1.
- [21] Tomas Möller and Ben Trumbore. "Fast, minimum storage ray/triangle intersection". In: *ACM SIGGRAPH 2005 Courses on - SIGGRAPH '05*. Vol. 2. 1. New York, New York, USA: ACM Press, 2005, p. 7. DOI: 10.1145/1198555.1198746.

- [22] JE Stone, David Gohara, and Guochun Shi. "OpenCL: A parallel programming standard for heterogeneous computing systems". In: *Computing in science & engineering* (2010). DOI: 10.1109/MCSE.2010.69.
- [27] G. A. De Jong, T. J. J. Maal, and H. Delye. "The computed cranial focal point". In: *Journal of Cranio-Maxillofacial Surgery* 43.9 (2015), pp. 1737–1742. ISSN: 18784119. DOI: 10.1016/j.jcms.2015.08.023.
- [28] United States Natick, Massachusetts. *Matlab 2015a*. Massachusetts, United States, 2015.
- [50] Erik Smistad, Anne C. Elster, and Frank Lindseth. "Real-Time Surface Extraction and Visualization of Medical Images using OpenCL and GPUs". In: *Nik-2012 november* (2012), pp. 141–152.
- [68] Minh-Bao Le et al. "Assessing long-term outcomes of open and endoscopic sagittal synostosis reconstruction using three-dimensional photography." In: *The Journal of craniofacial surgery* 25.2 (2014), pp. 573–6. ISSN: 1536-3732. DOI: 10.1097/SCS.0000000000000613.
- [69] Cheryl A. Hill et al. "Intracranial volume and whole brain volume in infants with unicoronal craniosynostosis". In: *Cleft Palate-Craniofacial Journal* 48.4 (2011), pp. 394–398. ISSN: 10556656. DOI: 10.1597/10-051.
- [70] D T Gault et al. *Intracranial pressure and intracranial volume in children with craniosynostosis*. 1992. DOI: 10.1097/00006534-199209000-00003. URL: <http://www.ncbi.nlm.nih.gov/pubmed/1513883>.
- [71] S Sgouros et al. "Intracranial volume change in craniosynostosis." In: *Journal of neurosurgery* 91 (1999), pp. 617–625. ISSN: 0022-3085. DOI: 10.3171/jns.1999.91.4.0617.
- [72] Daniel Saiepour et al. "Posterior cranial distraction in the treatment of craniosynostosis - Effects on intracranial volume". In: *European Journal of Plastic Surgery* 36.11 (2013), pp. 679–684. ISSN: 0930343X. DOI: 10.1007/s00238-013-0874-8.
- [73] Marie-Lise C. van Veelen et al. "Volume measurements on three-dimensional photogrammetry after extended strip versus total cranial remodeling for sagittal synostosis: A comparative cohort study". In: *Journal of Cranio-Maxillofacial Surgery* m (2016). ISSN: 10105182. DOI: 10.1016/j.jcms.2016.07.029.

8 | General Discussion

The goal of this thesis was to create a method for quantification of the human head evolution based on 3D photogrammetry. Both the normal evolution of the human head as well as the evolution of the head after craniosynostosis could be done using CT-scans. These however introduce ionizing radiation. The use of 3D photos results in losing the knowledge of the bony tissue used in normal sequential follow-up. Thus the CCFP was introduced as a new reference point for 3D photos or CT-scans similar to the existing reference point of the sella turcica in CT-scans or x-rays.

The initial CCFP computation had some compromises to deal with. Most of the technical compromises were solved in [Sections 3,4,5]. One important issue remained: the lack of a large data set. During the study a data set was acquired for pediatric CT-scans. The pediatric set was of greater importance since these would function as a reference for the 3D photos for the craniosynostosis set. Most other studies utilizing pediatric CT-scans are also limited on the amount of CT-scans available [12, 13, 58]. This is also the case for the amount of 3D Photos [74, 73].

During the revision of the CCFP computation in [Section 5] the effect of the amount of details on the CCFP position was also examined. Furthermore sampling was introduced by using raycasting [21]. Raycasting allowed expressing a mesh (like a 3D Photo) as a function of ray lengths in a hemi-ico sphere. Using this form of storage helps with shape comparison and shape evaluation.

Another important point in [Section 5] is the registration. The registration process of CT-scans is still partially performed manually. This could be done automatically [75, 63, 64]. Fully automatic registration procedures for CT-scans are not part of this thesis but will be implemented in the future. Automatic registration for 3D Photos is also planned. The lack of clear reference points on the mesh of the 3D Photo for automatic registration make the process more difficult compared to CT-scans. This however can be compensated for by the use of the 3D photo texture.

Luckily in the normal pediatric population there is only a few millimeter change in the mean CCFP position over age [Section 6]. The strongest changes occur in the first 15 months

of age. These CCFP values per age can be used as a correction. These corrections were used in [Section 7]. The effects of craniosynostosis on the CCFP are still not yet validated in real world cases. However in the synthetic cases of extreme trigonocephaly there was only a few millimeter difference in the CCFP position [Section 2].

As a final step the radiation-free 3D head shape and volume evaluation after endoscopically assisted strip craniectomy followed by helmet therapy for trigonocephaly was performed [Section 7]. Compromises had to be made due to limitations in the availability of both usable CT-scans of trigonocephaly patients as well as 3D photos of healthy children in the corresponding age groups. For the volume change over time only the pattern was compared between the healthy group (CT-scans) and craniosynostosis group (3D Photos). Furthermore the shape changes over time for the craniosynostosis group could not be compared to a healthy counterpart. Both for the CT-scans of craniosynostosis children as well as the 3D photos a database is made for future comparison.

All the tools for quantification of normal evolution of the human head in order to develop new craniosynostosis measurements are available. The actual evaluation is hindered by the lack of source data to create normal references. CT-scans and 3D photos to further expand the evaluation are collected for future evaluations.

The use of 3D photos could also help in the diagnosis of craniosynostosis. The full extend of the use of 3D photos as diagnosis measure are yet to be explored. The CCFP could assist in positioning the 3D photos in a reference frame. Analysis and comparison of 3D photos for children that are suspected for craniosynostosis with healthy references could give insight in the usefulnesses.

Using an objective measure significantly helps in the evaluation and quantification of the effects of craniosynostosis interventions. This is not only the case for our institution, but also for others around the world performing craniosynostosis interventions. The current 3D camera systems are getting cheaper and more available for both the mainstream and professional clients. Using these 3D cameras can help with reducing the amount of preventable ionizing radiation that is used in craniosynostosis follow-up.

References

- [12] Nikoo R Saber et al. "Generation of normative pediatric skull models for use in cranial vault remodeling procedures." In: *Child's nervous system : ChNS : official journal of the International Society for Pediatric Neurosurgery* 28.3 (2012), pp. 405–10. ISSN: 1433-0350. DOI: 10.1007/s00381-011-1630-7.

- [13] Hans Delye et al. "Creating a normative database of age-specific 3D geometrical data, bone density, and bone thickness of the developing skull: a pilot study". In: *Journal of Neurosurgery: Pediatrics* 16.6 (2015), pp. 687–702. ISSN: 1933-0707. DOI: 10.3171/2015.4.PEDS1493.
- [21] Tomas Möller and Ben Trumbore. "Fast, minimum storage ray/triangle intersection". In: *ACM SIGGRAPH 2005 Courses on - SIGGRAPH '05*. Vol. 2. 1. New York, New York, USA: ACM Press, 2005, p. 7. DOI: 10.1145/1198555.1198746.
- [58] M L Tolhuisen et al. "A Method for the Creation of Normative Paediatric Skull Models : A Pilot Study". In: *International Journal of Engineering Science and Innovative Technology* 3.6 (2014), pp. 1–7.
- [63] Kun Zhang, Yuan Cheng, and Wee Kheng Leow. "Dense correspondence of skull models by automatic detection of anatomical landmarks". In: *Lecture Notes in Computer Science (including subseries Lecture Notes in Artificial Intelligence and Lecture Notes in Bioinformatics)* 8047 LNCS.PART 1 (2013), pp. 229–236. ISSN: 03029743. DOI: 10.1007/978-3-642-40261-6_27.
- [64] Yuan Cheng, Wee Kheng Leow, and Thiam Chye Lim. "Automatic identification of Frankfurt plane and mid-sagittal plane of skull". In: *Proceedings of IEEE Workshop on Applications of Computer Vision* (2012), pp. 233–238. ISSN: 21583978. DOI: 10.1109/WACV.2012.6162994.
- [73] Marie-Lise C. van Veelen et al. "Volume measurements on three-dimensional photogrammetry after extended strip versus total cranial remodeling for sagittal synostosis: A comparative cohort study". In: *Journal of Cranio-Maxillofacial Surgery* m (2016). ISSN: 10105182. DOI: 10.1016/j.jcms.2016.07.029.
- [74] Hans Delye et al. "Endoscopically assisted craniosynostose surgery: the Craniofacial Team Nijmegen experience." In: *Journal of Cranio-Maxillo-Facial Surgery* (2016).
- [75] Zhong Yu. "Intrinsic shape signatures: A shape descriptor for 3D object recognition". In: *2009 IEEE 12th International Conference on Computer Vision Workshops, ICCV Workshops 2009* (2009), pp. 689–696. DOI: 10.1109/ICCVW.2009.5457637.

9 | Acknowledgments

The aging of wine is potentially able to improve the quality of wine. I truly hope that this aging effect also improves the quality of myself as an academic. At almost 10 years of studying technical medicine, having fun, working, finding goals to focus on I may finally present this thesis. There are many people I want to thank for the entire process and the last one and a half year at the neurosurgery department in particular. There are many more people I want to thank than I can enumerate in this acknowledgment.

First of all I want to thank my medical supervisor Hans Delye for the guidance and putting up the patience of working with me. In depth conversations about the thesis as well as many other aspects of neurosurgery and beyond always inspired me to work even harder. I shall never forget rule number one: "Hans is always right" (even when he is not). The congresses, movies, team dinners added great value to this internship for which I am very thankful.

Hans was also in some way my technical supervisor. But of course I want to thank Ferdi van der Heijden and Thomas Maal for being my technical supervisors. You all knew when to slow me down or keep in touch with the audience whenever I got too technical.

I want to thank Manon Tolhuisen for being a great college and a great friend. I will certainly miss the near weekly dinners, great cooking, and relaxing moment by the time you move away from Nijmegen.

The entire neurosurgical department and research corner made me feel very welcome from the start. I hope for a bright future with my colleagues with a lot of inspiring research.

One person that initiated the journey in technical medicine is Leon Massuger. I want to thank him for sending me in the direction of technical medicine.

A great guide during my study was Marieke Hofman. As a study adviser she helped me to give direction during the chaotic route I followed in technical medicine.

I want to thank my aunt Ignes for helping me at various moments during the master phase of the study. These moments greatly helped to kickstart my internships. And I *will* get you a new plant!

I want to thank my friends (you know who you are) for making my study a lot of fun, maybe making the study itself somewhat longer while making it look a lot shorter.

Thank you (little) sister for being able to crash in for dinner at nearly any time.

Most importantly I deeply want to thank my parents for ever supporting me throughout the entire process and always being there for me. I have no idea how I can ever repay this incredible support, but some day I will find a way.

Furthermore thank you all who I forgot to mention for now but deserve my thanks

Guido de Jong

August 2016